Re-appearance of precipitated aragonite crystal fans as evidence for expansion of oceanic dissolved inorganic carbon reservoir in the aftermath of the Lomagundi-Jatuli Event

Guang Ouyang [a, b], Zhenbing She [a*], Qian Xiao [a], Kenan Cao [a], Zongyuan Ran [a], Tao Hu [a], Genming Luo [a], Dominic Papineau [a, c, d, e], Chao Li [f, g]

[a] State Key Laboratory of Biogeology and Environmental Geology, School of Earth Sciences, China University of Geosciences, Wuhan, China

[b] Third Institute of Oceanography, Ministry of Natural Resources, Xiamen, China

[c] London Centre for Nanotechnology, University College London, London, UK

[d] Department of Earth Sciences, University College London, London, UK

[e] Centre for Planetary Science, University College London and Birkbeck College, London, UK

[f] State Key Laboratory of Oil and Gas Reservoir Geology and Exploitation & Institute of Sedimentary Geology, Chengdu University of Technology, Chengdu 610059, China

[g] Key Laboratory of Deep-time Geography and Environment Reconstruction and Applications of Ministry of Natural Resources, Chengdu University of Technology, Chengdu 610059, China

ABSTRACT

The initial accumulation of atmospheric oxygen is marked by the unprecedented positive $\delta^{13}C_{carb}$ excursions of the Lomagundi-Jatuli Event (LJE) and records an interval of abnormal O_2 production through elevated rates of organic carbon burial. Emerging evidence suggests that the post-LJE atmosphere-ocean system might have suffered a significant deoxygenation. These dynamic perturbations in the oceanic redox state and biogeochemical cycles would have led to fundamental changes in carbonate precipitation dynamics. Here, we report the discovery of centimeter-sized crystal fans in the post-LJE Huaiyincun Formation, Hutuo Supergroup in the North China Craton. The hexagonal cross-sections and square terminations suggest that these fan-like dolomitic structures were originally aragonite crystal fans (ACF). Variations of stromatolite morphology and frequent occurrences of storm-related deposits in the Huaiyincun Formation point to repeated cycles of sea level changes. The bedding-parallel distribution of the ACF and the homogeneous $\delta^{13}C$ values of the ACF-bearing dolostones are consistent with a primary depositional origin for the ACF. An updated compilation of published records of ACF throughout geological history highlights a clear absence of ACF from the initiation of the Paleoproterozoic Great Oxidation Event until the end of the LJE, and a global reappearance of ACF in the post - LJE late Paleoproterozoic. We propose that the reappearance of ACF is in agreement with the expansion of the oceanic dissolved inorganic carbon (DIC) reservoir. At the same time, consumption of dissolved oxygen during the oxidation of organic matter might have been stimulated by ferruginous deep seawater, facilitating the formation of Huiayincun ACF.

Key words: Lomagundi-Jatuli Event; Great Oxidation Event; seafloor precipitates; dissolved inorganic carbon, Hutuo Supergroup

1. INTRODUCTION

The first accumulation of oxygen in the atmosphere between 2.43 - 2.06 Ga (Great Oxidation Event, GOE) is evidenced first by the disappearance of oxygen-sensitive detrital minerals such as pyrite and uraninite along with the appearance of Fe-rich paleosols in the sedimentary record (e.g., Holland, 2002). The precise timing of this event is constrained by the termination of mass independent fractionation of sulfur isotope (e.g., Farquhar et al., 2000; Papineau et al., 2005a, 2007; Luo et al., 2016; Poulton et al., 2021; Izon et al., 2022). The rise of oxygen levels in the Paleoproterozoic atmosphere would have led to an episode of extensive continental weathering and oxidation of shallow seawater (Bekker et al., 2004; Kump, 2008; Luo et al., 2016), followed by a series of unprecedented events, including the largest positive excursions of carbonate carbon isotope composition ($\delta^{13}C_{carb}$) in Earth's history (known as the Lomagundi - Jatuli Event, LJE) (Galimov et al., 1968; Schidlowski et al., 1976; Martin et al., 2013). However, abrupt negative $\delta^{13}C_{carb}$ excursions occur in strata post - dating the LJE, which have been interpreted as the result of massive oxidation of organic matter with significant changes in the ocean - atmospheric redox state (e.g., Kump et al., 2011; Papineau et al., 2017).

Authigenic carbonate precipitates can provide important information about the evolution of ocean chemistry as they precipitate directly from seawater (Kastner, 1999; Cantine et al., 2020). Aragonite crystal fans (ACF) are fan-shaped aggregates of acicular aragonite that are generally interpreted as *in situ* seafloor precipitates (Grotzinger and James, 2000; Bergmann et al., 2013). The oldest ACF reported so far are preserved in the 3.35 Ga Strelley Pool Formation in the Pilbara Craton of Western Australia, along with some of the oldest known stromatolites (Grotzinger, 1989; Allwood et al., 2009). Similar fan-like structures have been reported from Archean, Paleoproterozoic and some Phanerozoic strata (Table 1) (e.g., Bergmann et al., 2013; Grotzinger and Knoll, 1995; Okubo et al., 2018; Woods, 2014). Formation of this unusual sedimentary fabric has been interpreted to result from upwelling in a redox-stratified ocean, producing mixing of deep anoxic and surface oxic waters (Grotzinger and Knoll, 1995). However, the traditional upwelling model has been questioned by recent studies on ACF at the Permian-Triassic boundary (PTB) because there is lack of abundant precipitated carbonate fans in most PTB microbialites, and the strong ocean stratification would have limited upwelling (Kershaw et al., 2012). In addition, the scattered temporal distribution of ACF in the sedimentary record could be partly attributed to preservational bias (Bergmann et al., 2013). Therefore, better understanding of the mechanism of ACF precipitation and its environmental significance requires more complete documentation of these seafloor precipitates throughout geological history.

Here we report abundant pseudomorphs of ACF in the 2.0 - 1.9 Ga Huaiyincun Formation of the Paleoproterozoic Hutuo Supergroup in the North China Craton. Previous studies have suggested that the carbonate rocks in the Huaiyincun Formation record dynamic changes in the carbon and sulfur cycles following the LJE (Ouyang et al., 2020). This, combined with a compilation of ACF in the sedimentary record, provides a unique window to elucidate environmental conditions during ACF formation, which in turn can offer insights into the chemical composition and dynamics of the shallow seawater during this critical period.

2. GEOLOGICAL SETTING

As one of the oldest cratons in the world, the North China Craton (NCC) underwent multiple stages of continental growth (Zhai et al., 2020) and has been divided into the Western Block, the Eastern Block and the central Trans-North China Orogen in between (Fig. 1; Zhao et al., 2001). The stabilization and cratonization of the NCC occurred in the latest Neoarchean, as evidenced by intensive magmatism and metamorphism at ~2.5 Ga (Zhai et al., 2000; Wan et al., 2011). This was followed by basement uplift and rift development during the

Paleoproterozoic in response to the assemblage and the subsequent breakup of the supercontinent Columbia (Zhao et al., 2003; Zhao et al., 2005).

The Hutuo Supergroup is well exposed in the Wutai area of the Trans - North China Orogen (Fig. 1B). It rests unconformably on the early Paleoproterozoic Gaofan Group or the Neoarchean Wutai Group. The Hutuo Supergroup has been subdivided into three groups in ascending order (Fig. 2): the Doucun Group, characterized by terrigenous clastic sediments with subordinate carbonates and volcanic interbeds; the Dongye Group, dominated by massive carbonate deposition; and the Guojiazhai Group, consisting exclusively of sandstone and conglomerate (Bai, 1986). The overall sedimentary pattern expressed by the Doucun and Dongye groups is one large-scale transgression (Ouyang et al., 2020; Bai, 1986).

The maximum age of the Hutuo Supergroup is constrained by a group of 2.14 Ga zircons in basaltic andesite from the bottom of the Doucun Group (Du et al., 2010). Ages of the youngest detrital zircons suggest that the Guojiazhai Group must have deposited after 1.919 Ga (Liu et al., 2011). Meanwhile, the minimum age of the Guojiazhai Group has been indirectly constrained by the crosscutting 1.78 - 1.75 Ga late Paleoproterozoic mafic dykes (Peng et al., 2005) and overlying 1.8 - 1.6 Ga Changcheng Group (Lu et al., 2008). Combined with other geochronological studies, the depositional age of the Hutuo Supergroup has been constrained between 2.14 Ga and 1.80 Ga (Fig. 2) (e.g. Wilde et al., 2004; Du et al., 2017), postdating the GOE. Carbon isotope chemostratigraphic data suggest that the Hutuo Supergroup recorded a characteristic termination of the 2.22 - 2.06 Ga LJE (She et al., 2016). Chen et al (2019) identified possible glaciogenic diamictites from the lower ~2.1 Ga Doucun Group, which are slightly younger than the ca. 2.40 - 2.25 Ga Huronian Glaciation Event. These results collectively suggest that sediments in the Hutuo Supergroup recorded the aftermath of the GOE.

The Dongye Group sits in the middle of the Hutuo Supergroup, consisting of, in ascending order, seven formations named Wenshan, Hebiancun, Jianancun, Daguandong, Huaiyincun, Beidaxing and Tianpengnao (Bai, 1986). The Huaiyincun Formation of the Dongye Group is best exposed at ca.1.5 km northwest of the Dongye Town, Xinzhou, Shanxi Province, China and is characterized by massive carbonate deposits. Sedimentological and carbonate mineralogical features of the Huaiyincun Formation were previously interpreted to record an overall transgression on the Dongye platform (Bai, 1986). As metasandstones collected from the underlying Hebiancun Formation containing a youngest group of zircons with ages around 2010 Ma (Liu et al., 2011), the depositional age of the Huaiyincun Formation can be roughly constrained between 2.0 and 1.8 Ga (discussed in Ouyang et al., 2020).

Two parallel sections, ~500 meters apart, of the ~200-m thick Huaiyincun Formation near Dongye have been investigated in this study (Fig. 1B). The Huaiyincun West section (GPS coordinates 38° 39′ 21″ N, 113° 7′ 9.63″ E to 38° 39′ 17.47″ N, 113° 7′ 9.74″ E) and the Huaiyincun East section (GPS coordinates 38° 39′ 23.95″ N, 113° 7′ 30.04″ E to 38° 39′ 14″ N, 113° 7′ 30.10″ E) display a very similar sedimentary sequence and can be readily correlated (Fig. 2). The Huaiyincun Formation consists of centimeter to decimeter - thick bedded dolostone, with subordinate columnar, branching and domal stromatolites. Dolostone intraclasts, hummocky cross stratification and graded bedding are common. One striking feature of the Huaiyincun Formation is the transition from pink dolostone in the lower part to the grey dolostone in the upper part, accompanied by the disappearance of stromatolites and increasing abundance of storm-related structures (Ouyang et al., 2020). A Previous mineralogical study of the Huaiyincun Formation revealed a decrease in iron oxides and detrital minerals and an increase in organic content along with the change in dolostone color from pink to grey, consistent with an overall deepening of water depth (Ouyang et al., 2020).

3. METHODS

This work is based on detailed field and petrologic observations. Stratigraphy and sedimentary features of the Huaiyincun west and east sections were described bed-by-bed at outcrops, with an emphasis on the paleoenvironment and its relationship with the development of ACF. These were augmented by mineralogical and compositional characterizations with Raman spectroscopy, electron probe micro-analysis, scanning electron microscopy, optical cathodoluminescence (CL) and isotope ratio mass spectrometry.

3.1 Sample Preparation and Optical Microscopy

Sixty samples were collected from the Huaiyincun Formation. All samples were taken from fresh outcrop and weathered surfaces were removed to reduce the impact of weathering on mineralogy and geochemical composition. A 28 cm × 20 cm crystal fan - bearing sample was polished along a bedding-normal plane, allowing for detailed investigation of the isotopic variation within and between the sedimentary laminae. Other samples were ground and polished to make 30 - μm - thick thin sections. Petrographic characterization of thin sections was conducted with a Zeiss Axio Scope A1 optical microscope at China University of Geosciences, Wuhan (CUG-Wuhan) equipped with 1.25×, 5×, 10×, 20×, 50× and 100× objectives in the transmitted and reflected light modes. Photomicrographs were taken with the AxioVision LE64 imaging system that controls a AxioCam MRc 5 (5 mega pixels) charge-coupled device camera.

3.2 Micro-Raman Spectroscopy

Micro - Raman imaging was conducted at the State Key Laboratory of Biogeology and Environmental Geology (BGEG), CUG-Wuhan with a WITec α300R confocal Raman imaging system. A 532 nm laser was used with a power maintained between 7 and 10 mW and focused with a 50× or 100× objective for both large and small area scans, achieving spatial resolutions between 2000 and 360 nm. A 50 μm diameter optic fiber was selected as a compromise for confocality and signal-to-noise ratio and a 600 grove/mm grating was used to provide a large bandwidth of 4000 cm^{-1} and a spectral resolution of 4 cm^{-1}. Samples were cleaned with ethanol and high purity nitrogen before analysis. The targets for Raman imaging were examined under reflected light to exclude areas of open cavities and popped - out grains that could have captured contaminants from polishing. The analysis was performed at least 0.5 μm below the sample surface to avoid surface contamination. All Raman spectra herein were generated by averaging pixels with nearly identical spectra and processed with the WITec Project Five software. Cosmic rays were removed under 2 cm^{-1} filter with a dynamic factor of 8. Then the background was subtracted by using polynomial functions with up to the 7th order. Minerals are shown coded in different colors according to their characteristic peaks.

3.3 Scanning Electron Microscopy and Energy Dispersive X-ray Spectrometry

Polished samples were also examined at BGEG with a TESCAN Vega 3 scanning electron microscope equipped with an Oxford X-act energy-dispersive X-ray spectrometer at BGEG. Analyses were performed on the samples under a vacuum pressure of 10^{-3} Pa with a 0.5 nA electron beam accelerated at 20 kV, with a working distance of 15 mm.

3.4 Electron Probe Micro-analysis

Mineral compositions for carbonate at target spots for micro - drilling were determined using a JEOL JXA-8100 electron probe micro-analyzer at the State Key Laboratory of Geological Processes and Mineral Resources, CUG-Wuhan. Selected thin sections were polished with 60 μm Al_2O_3 powder, cleaned with ethanol and dried using high purity nitrogen, and then coated with a thin layer of gold. Wavelength dispersive spectroscopic analyses were performed to determine the concentration of major carbonate cations. Conditions for the primary electrons included an accelerating voltage of 15 kV, a beam current of 10 nA, and a 5 μm focused beam, whereas the counting time for each analysis was 30 s. Standardisation on diopside (Ca) and olivine (Mg and Fe) gave a reproducibility better than 0.5 wt%. Both standards are from SPI Supplies.

3.5 Cathodoluminescence

CL imaging for thin sections of the ACF - bearing samples were performed with a CITL CL8200-MK5 cathodoluminoscope attached to a Leica DFC300FX photomicroscope. The sample chamber was kept under partial vacuum at 0.003 mbar and analyses were operated at approximately 10 kV with a 0.5 mA beam current.

3.6 Carbon and Oxygen Isotope Analysis

Fifteen samples were micro-drilled from a polished slab to characterize the carbon and oxygen isotopic variation between ACF pseudomorphs and their surrounding matrix. This region was selected because of its structural integrity and lack of secondary veins and cracks. Measurement was performed on a Gas Bench II-MAT253 at BGEG following previously described analytical procedures (Song et al., 2014). Results were corrected based on the NBS19 standard and reported in permil (‰) relative to the Vienna-Pee Dee Belemnite (V-PDB) standard. External reproducibility was better than 0.06‰ for $\delta^{13}C$ and 0.1‰ for $\delta^{18}O$ (1σ) based on duplicate analyses.

4. RESULTS

4.1 Sedimentary Features of the Huaiyincun Formation

The lower Huaiyincun unit is dominated by pink dolostone, and storm-related features only occasionally occur within a few centimeter- to decimeter- thick beds (Fig. 3). The intraclasts are unsorted and angular in shape and are lithologically identical to the underlying or coeval dolostones (Figs. 3A-C). Scour structures associated with intraclasts and normal graded bedding can be observed in the middle of the pink dolostone unit (Figs. 3D and 3E). Hummocky cross stratification appears at the top of the lower pink dolostone unit. The hummocky cross-stratified beds are ~20 cm thick and the height of the hummocks is~3 cm (Fig. 3F). Apart from these, the lower pink unit is dominated by fair - weather deposits such as stromatolitic dolostone (Fig. 4). In comparison, the upper grey unit of the Huaiyincun Formation is characterized by thick bedded dolostone with storm - related sedimentary structures including intraclasts, graded bedding and hummocky cross stratification (Ouyang et al., 2020).

Four distinct morphotypes of stromatolites can be recognized from the outcrop of the lower pink unit of the Huaiyincun Formation: coniform form, columnar form, wavy form and meter - scale domal bioherm. The coniform stromatolites occur near the base of the lower pink unit, usually present as lenticular bodies that are less abundant and smaller in size compared to the other forms (Fig. 4A-B). The thickness of the coniform laminations is ~0.5 mm and the maximal height and width of a single cone is ~2 cm and 3 cm, respectively. Synoptic relief of the coniform laminae increases from bottom to top and reach the highest of ~1cm, which is morphologically similar to other stromatolites reported from the Paleoproterozoic Wooly Dolomite (Nutman et al., 2016). Wavy stromatolites have gently convex laminations composed of carbonate and are laterally continuous (Fig. 4C). The thickness of the wavy stromatolites is over 50cm with the synoptic relief of ~0.3cm (Fig. 4E), and most of the wavy stromatolites are found in close proximity to the columnar stromatolites (Figs. 4E and F). Columnar stromatolites occur either as independent columns or as branched ones, with axes perpendicular to the bedding plane (Fig. 4D). The columns are up to ~30 cm in height and 0.7-1.3 cm in width, synoptic relief is similar to those in the wavy stromatolites. Stromatolite bioherms (Fig. 4G) are observed in two horizons in the west section of the Huaiyincun Formation but only one horizon in the east section of the formation (Fig. 2). The diameter of the bioherms can be up to 5 m while the laminations are ~1 to 10 cm thick. In fact, the bioherms often consist of subordinate columnar and wavy stromatolites, which appear darker than the intercolumn deposits on weathered surfaces (Fig. 4G). It is also noted that dolomitic intraclasts are occasionally observed within stromatolite laminae (Fig. 3C).

Oolites occur below the upper bioherm section in the east profile of the Huaiyincun Formation (Fig. 2). The ~20 cm oolitic layer is underlain by a ~1.2m thick intraclastic bed (Fig. 5A and 5B), in which the intraclasts are unsorted with variable sizes ranging from 0.5 mm to 4 mm (Fig. 5C). Ooids are millimeter-scale, circularly concentric and their radially aligned dolomite crystals also exhibit grey colour gradient (Fig. 5D). The nuclei of ooids are comprised of micritic dolomite, often darker in color (Fig. 5E).

Dolomitized ACF are present in multiple horizons in the lower pink unit of Huaiyincun Formation (Fig. 2) and are observed after the first appearance of meter-sized bioherms (Figs. 6A and 6B). ACF - bearing layers are sometimes found interbedded with fine - grained, hummocky cross - stratified dolostones (Fig. 6H), consistent with the storm - related structures in the lower pink unit of the Huaiyincun Formation. Distinct ACF - bearing layers interbedded with centimeter - sized banded dolostone are also observed, with thicknesses of single layers ranging from 0.5 cm to 5 cm (Fig. 6C - 6E). Some of the ACF are found upside down, whereas the other ACF and stromatolitic laminae remain undisturbed.

4.2 Morphology and Mineralogy of the ACF

ACF clusters are typically 1-2 cm across and feature a radiating arrangement of carbonate needles that are best observed on weathered surfaces perpendicular to the bedding plane (Fig. 6C) and sometimes on the top surface of the bedding plane (Fig. 6F). Centimeter - thick layers of fans commonly have irregular upper and lower bounding surfaces, although flat bottoms are also observed (Figs. 6C - 6E). ACF - bearing layers are sometimes found interbedded with fine - grained, hummocky cross - stratified dolostones (Fig. 6H).

ACF can be easily observed under the petrographic microscope. While the ACF have been completely dolomitized, their crystals are distinctly clearer than the surrounding dolomite matrix under the transmitted light (Figs. 7A and 7B). The acicular crystal pseudomorphs in the ACF range in width from 0.3 mm to 1 mm. The length of most needles is ~5 mm with an average length-width ratio of ~10:1. It should be noted that these values are likely underestimates owing to their randomized cut lengths in thin sections. Therefore, the true dimension of these needles should be larger, which is consistent with field observations. Individual needles are characterized by square terminations (Fig. 7C) and hexagonal cross-sections (Fig. 7D). Notably, co - occurrence of ACF and millimeter - scale stromatolites are sometimes observed under the microscope (Fig. 7E).

EDS elemental maps document complete dolomitization of the ACF. They show relative depletion in Ca and Mg and enrichment in Al and Si in the interstitial matrix compared with the crystal pseudomorphs (Fig. 8). This is consistent with the result of high - resolution Raman imaging that shows the relative enrichment of clay minerals, quartz, and hematite in interstitial micritic matrix (Fig. 9). CL imaging shows distinct luminescent inter-needle matrix and dully luminescent of ACF (Fig. 10).

4.3 Geochemistry of the ACF

Carbonate carbon and oxygen isotope data from 15 sub - samples micro - drilled from the polished slab of ACF - bearing dolostone are given in Table 2 and plotted in Fig.11A. The overall $\delta^{13}C_{carb}$ values range tightly between +0.1‰ to +0.3‰ (V-PDB), with an average value of +0.2‰ (n=15). $\delta^{18}O_{carb}$ values of the micro-drilled samples range from -6.3‰ to -6.8‰, with an average of -6.5‰ (n=15). Both the carbon and oxygen isotope compositions show negligible variations between the crystal fans and the matrix spots, with average values of +0.2‰ (n=9) vs. +0.2‰ (n=6) for $\delta^{13}C_{carb}$ and -6.5‰ versus -6.7‰ for $\delta^{18}O_{carb}$. There is also no significant correlation between $\delta^{13}C_{carb}$ and $\delta^{18}O_{carb}$ values (Fig. 11B). Total mass of the major element analysis is constant to around 100 wt%, except drill spot 2 (Table 2). Drill spot 2 and its repetition show unusual total oxide contents of 106.7 wt% and 108.1 wt%, together with distinctly higher SiO_2 contents of 9.5 wt% and 12.9 wt%. FeO content ranges from 0.4 to 0.8 wt%. MgO and CaO contents vary from 19.0 to 21.0 wt% and 25.0 - 29.7 wt%. Mg/Ca mole ratios of the drill spots vary between 0.97 to 1.18 with an average value of 1.01. Neither compositional variations across the laminae nor a correlation between Mg/Ca and $\delta^{13}C_{carb}$ values is observed (Fig. 11C).

5. DISCUSSION

5.1 Depositional Environment of the Huaiyincun Formation

The occurrence of stromatolites and storm-related structures in the lower Huaiyincun pink dolostones documents a generally shallow environment with intermittent high - energy events (storms). The lower limit of water depth for carbonate stromatolite formation was estimated at ~50 - 80 m (Turner et al., 2000; Kah et al., 2006), although diverse microbial communities and various depositional environments might result in different stromatolite morphotypes (Papineau et al., 2005b). The axes of the conical stromatolites are progressively inclined upward (Fig. 4A), consistent with the phototaxis behavior of stromatolite - building microorganisms during seasonal variations in the direction of incident solar radiation (Vanyo and Awramik, 1985). However, this is unlikely the case for the Huaiyincun Formation because the immediately overlying columnar stromatolites do not show the same feature (Fig. 4D). Instead, the conical stromatolites with inclined axes could also be the result of competition between neighboring structures for near - shore nutrients (Petroff et al., 2010). The relatively high synoptic relief of the conical laminae compared to other stromatolites in the Huaiyincun Formation suggests that they sat quite high above the seafloor (Fig. 4A). It is notable that the conical stromatolites commonly occur as lenticular bodies within the dolostone bed (Fig. 4B), likely as a result of rapid burial in a low energy environment below the fair weather wave base. Intraclasts within the conical laminae are tabular and horizontally aligned (Fig. 4A), indicating the disturbance of occasional storm events. These observations suggest that the conical stromatolite in the Huaiyincun Formation developed between the storm wave base and the fair weather wave base. Similar structures observed in Archean sediments from the Beilingwe Greenstone Belt of Zimbabwe, the Quartzite lake area of northwest Canada and the Pilbara Craton of Australia were also proposed to have deposited in shallow marine environment (Martin et al., 1980; Walter et al., 1980; Hofmann and Davidson, 1998; Allwood et al., 2006;Coffey et al., 2013).

Further upsection, the gently convex wavy stromatolites (Fig. 4C) are consistent with the development of cyanobacterial communities in a subtidal environment with limited physical disturbance and sufficient supply of sunlight (Andres and Reid, 2006; Caird et al., 2017). The dense laminae and absence of intraclasts further support that these wavy stromatolites developed in a calm depositional environment, likely below the fair weather wave base. Columnar stromatolites commonly grew tightly next to each other to resist against the influence of tides (Logan et al., 1964). However, columnar stromatolites in the lower Huaiyincun Formation are independently erected, and barely disturbed (Fig. 4D), indicating growth in relatively low - energy environments with sufficient space. The low synoptic relief and successive alternations of columnar stromatolites and wavy stromatolites suggest that they grew under similar water depth and never stood high above the seafloor. Considering the absence of the structures that can be related to competition for resources (such as the inclined axes of the conical stromatolites), we propose that the wavy and columnar stromatolites developed in a relatively shallower environment than the conical ones. The meter - scale low - relief bioherms in the lower Huaiyincun Formation internally composed of wavy and columnar - laminated stromatolites (Fig. 4G). Such a low - relief domal characteristic associated with disturbed sediments filling between the inner stromatolitic columns (Fig. 4H) is commonly related to the intertidal to shallow subtidal environment (Kah et al., 2009), likely above the fair weather wave - base. The absence of evaporative mineral and mud cracks in the Huaiyincun bioherms suggests negligible subaerial exposure during their formation. Further upsection, reappearances of columnar and wavy stromatolites (Fig. 2), following the first bioherms section suggest an increase of seawater depth.

Oolites below the upper bioherms section of the east Huaiyincun Formation likely represent deposition above the fair weather base. The accumulations of ooids suggests that the agitated seawater reached supersaturation with respect to calcium carbonate (Strasser, 1986; Corsetti et al., 2006). Ooid nuclei have the same mineralogy as the underlying dolostone clasts, both being micritic dolomite without detrital minerals (Figs. 5C and 5D). These observations suggest that the Huaiyincun ooids formed with little contribution from terrestrial input.

Collectively, the sedimentology of the lower Huaiyincun Formation characterizes fluctuations of water depth (Figs.2 and 12), beginning with the shallowing of seawater as represented by the evolution of stromatolite morphology from coniform to columnar / wavy and then domal. A subsequent, slight rise of sea level led to the reappearances of columnar and wavy stromatolites, followed by a decline as suggested by the occurrence of oolites and a second layer of bioherms. Eventually, the sea level rose dramatically in the uppermost part of the lower Huaiyincun Formation.

5.2 Primary versus Post-depositional Origins for the Huaiyincun ACF

Although the crystal fans in the Huaiyincun Formation have been completely dolomitized, the characteristic textures of square terminations and hexagonal cross - sections point to an original aragonite mineralogy (Figs. 7C and 7D). The origin of the ACF should be discussed considering that fan - like calcite textures sometimes form after sediment deposition (Greene et al., 2012; Kershaw and Guo, 2016) and are sometimes primary depositional features. The way that crystal fans contact with the laminae and the surrounding matrix provides a first order judgement for their origin. Unlike those post - depositional botryoidal aragonites with inner fan

- like textures (e.g., Cui et al., 2019), the Huaiyincun ACF occur in thin layers that are parallel to the bedding plane (Fig. 6B and 6E). The flat lower bounding surfaces of ACF indicate that these crystal fans developed in a calm environment, where the micritic dolomite groundmass precipitated from the water column and filled the inter-needle spaces (Winefield, 2000). This is also supported by the co - occurrence of ACF and centimeter - scale stromatolites observed in the Huaiyincun Formation (Fig. 7E). It is notable that the occurrence of the ACF follows the domal stromatolites during the rise of sea level (Fig. 2). Meanwhile, hummocky cross - stratification in association with ACF (Fig. 6H) suggests that the ACF formed above the storm wave base. The distinct inter - needle spaces are also different from those tightly stacked ACF formed after deposition of sediment (Greene et al., 2012; Kershaw and Guo, 2016). Interestingly, layers with tilted or overturned ACF are present (Fig. 6G), probably as a result of disturbance during storm events or of nucleation on non-horizontal surface.

In the CL images, the crystal fans show distinctly duller luminescence compared with the surrounding dolomitic matrix (Fig. 10). Considering that manganese and iron are the most important activator and quencher, respectively, for CL in carbonate minerals (Pierson, 1981), the difference in luminescence suggests that the crystal fans have relatively high Fe/Mn ratios compared to the surrounding matrix. Similar CL characteristics were also reported in other ACF such as the Neoproterozoic Trezona Formation where originally aragonitic cements make very think, non - luminescent crusts of fibrous crystals with square terminations (Hood and Wallace, 2018).

Post - depositional crystal fans can also be identified through their carbon isotopic characteristics, with post - depositional fans typically showing a high degree of isotopic variability (Pruss et al., 2008; Heindel et al., 2015). This is because the $\delta^{13}C_{carb}$ values of the diagenetic fluids are generally different from that of the overlying seawater. Besides, even if these fans were formed under the sediment-water interface during the early diagenesis, differential organic matter remineralization and slow diffusion within sediments could also lead to heterogeneity in the carbon isotopic composition (Hennessy and Knauth, 1985; Irwin et al., 1977; Mazzullo, 2000). The absence of a strong covariation between $\delta^{13}C_{carb}$ and $\delta^{18}O_{carb}$ versus Mg/Ca (Figs. 11B and 11C) indicates insignificant overprint of the isotopic composition by dolomitization and other post - depositional processes. More importantly, $\delta^{13}C_{carb}$ values of the crystal fans from different laminae are relatively homogeneous and are indistinguishable from those of the surrounding matrix (Fig. 11A), consistent with the carbon isotope curve of the entire Huaiyincun Formation (Ouyang et al., 2020). Collectively, petrological, sedimentological and geochemical observations document that the Huaiyincun crystal fans are dolomitized seafloor aragonite precipitates and that they preserved the isotopic composition of contemporaneous seawater.

5.3 Formation Mechanism of the Huaiyincun ACF

In the Huaiyincun Formation, ACF are absent within the intervals of sea level drop and are best developed during transgression. Similarly, in the coeval Nash Fork Formation of the Snowy Pass Supergroup in Wyoming, USA, centimeter - sized crystal fans occurred shortly after the drowning of a carbonate platforms in the aftermath of the LJE (Bekker and Eriksson, 2003). Such relationships can also be found in many other Archean to Proterozoic crystal fan-bearing carbonates for which transgression has generally been invoked as the main factor that promoted the formation of ACF (Bergmann et al., 2013; Viehmann et al., 2020; Winefield, 2000). It is worth noting that the ACF of the Huaiyincun Formation commonly occur following the rise of sea level (Fig. 2). Also as evidenced by a dramatic decline of stromatolites and detrital input (Bai, 1986, Ouyang et al., 2020), the Huaiyincun Formation recorded a significant transgression event that led to the drowning of the Dongye carbonate platform, and thus represents the maximum flooding interval in the Hutuo Supergroup. During this transgression, upwelling of deep anoxic water would have caused a rise in alkalinity and lead to carbonate oversaturation in shallow oxic water, which in turn would have created a favorable environment for aragonite nucleation and growth on the seafloor (Woods et al., 1999).

The formation of ACF on the seafloor has also been suggested to require the presence of Fe^{2+} as an inhibitor to the precipitation of carbonate micrite (Okubo et al., 2018; Pruss et al., 2008; Winefield, 2000; De Leeuw, 2002). Anaerobic oxidation of organic matter involving ferric iron could have increased the pH and released Fe^{2+} (equation 1), creating a suitable environment for ACF formation:

$$(CH_2O)_n + 4n\, Fe^{3+}(OH)_3 + 7n\, CO_2 \rightarrow 8n\, HCO_3^- + 4n\, Fe^{2+} + 3n\, H_2O \text{ (equation 1)}$$

This is consistent with the presence of hematite in interstitial micritic matrix between the ACF as revealed by Raman imaging and higher Fe/Mn ratios of the ACF suggested by CL (Figs. 9 and 10). The abundant ferric oxide could act as the electron acceptor during the anaerobic oxidation of organic matter, which also explains the low abundance of the organic matter in the ACF - bearing samples. Sustained upwellings might be another source of iron and lead to the deposition of hematite on the shallow seafloor. Meanwhile, oxidation of Fe^{2+} and the mixture of the deep anoxic upwellings would greatly consume the free oxygen in shallow ocean, produce redox-sensitive ferric - ferrous iron and thus facilitate the oxidation of organic matter. Besides, the co - occurrence of ACF and the stromatolites in the Huaiyincun Formation (Figs. 6A and 6B) is not unique and a rather common phenomenon. Similar features can be found in many other ACF-bearing strata from Archean to Phanerozoic (e.g., Hofmann and Jackson, 1987; Kiyokawa et al., 2006; Pruss et al., 2008; Allwood et al., 2009; Friesenbichler et al., 2018), which implies a close relationship between microbial activity and the growth of ACF. Meanwhile, the extremely low seawater sulfate concentration during the Huaiyincun deposition (discussed in Ouyang et al., 2020) would have inhibited bacterial sulfate reduction, preventing the scavenging of dissolved Fe^{2+}. Ultimately, in the presence of reduced iron and oversaturation of carbonate, an optimal environment for ACF formation can be created.

Besides the environmental conditions for ACF formation, the types of chemical reactions that may lead to the formation of mineral patterns in ACF and ooids will now be considered briefly. The circular concentricity and the radial alignment of the dolomitized needles of ACF and ooids is a pattern that also occurs in botryoidal minerals, which are usually considered to be diagenetic and abiotic in origin (Papineau et al., 2021). Raman spectroscopy has been used to identify phases in circularly concentric botryoids and granules, and here in ACF, however there are only a few similarities between these objects, such as the presence of Fe^{2+} - bearing hematite and anatase (Papineau et al., 2017). The low abundance of organic matter in the Huaiyincun ACF suggests that most microbial organic matter may have been oxidized, however this is not supported by the seawater - like carbon isotope ratios of dolomite and can hardly be demonstrated. The inferred low level of seawater sulfate during the deposition of the Huaiyincun formation is also not immediately supportive of chemically oscillating reactions, some of which require sulfuric acid, and which have recently been proposed to explain such mineral patterns (Papineau, 2020; Papineau et al., 2021). However, the range of conditions under which chemically oscillating reactions can produce circularly concentric patterns that radially expand is not known and therefore this model may find more support by future analyses of trace elements in ACF and more varied experiments.

5.4 ACF in the Sedimentary Record

Inorganic aragonite precipitates have been observed in modern environments with the presence of microbialites and stromatolites, such as the Persian Gulf and the Great Bahamas Bank respectively, in the form of fibrous cement in ooids and independent needles (Grammer et al., 1999; Turpin et al., 2011), and even in subglacial carbonate crusts in the Alps (Thomazo et al., 2017). However, fan - like aragonite clusters with flat bases are absent on the modern seafloor. One possible explanation is that anoxic, Fe^{2+} rich conditions cannot persist in the fully oxygenated and ventilated modern oceans.

Despite their rarity in the Phanerozoic, ACF are widely reported from horizons near the Permian - Triassic boundary that features the largest mass extinction in Earth history (Fig. 13A; Table 1; Baud et al., 2007; Friesenbichler et al., 2018; Heindel et al., 2018; Heydari et al., 2003; Richoz et al., 2010; Woods et al., 2007; Woods and Baud, 2008; Chen et al., 2010; Pruss et al., 2005; Woods et al., 1999). This unique phenomenon in the Phanerozoic has even been recognized as an "anachronistic facies" because it is similar to those in Precambrian carbonates (Wignall and Twitchett, 1999; Woods, 2014). Most of these crystal fans are thought to have formed in the outer shelf environments and to have been closely associated with microbialites (Woods, 2014). Grotzinger and Knoll (1995) proposed that the ACF at the Permian - Triassic boundary are related to upwellings of anoxic, alkaline bottom water. Indeed, numerous studies have documented a significant expansion of the oxygen minimum zone and extensive anoxia in the coeval shallow seawater (e.g., Algeo et al., 2011; Winguth and Winguth, 2012).

The reports of ACF then become scarce in the Neoproterozoic (Fig. 13A). With the exception of several reports from the Ediacaran Dengying Formation (Cui et al., 2019), most of the fan - like carbonate structures found in the Neoproterozoic are preserved in post - glacial sediments (e.g., Nogueira et al., 2003; Clough and Goldhammer, 2000; Hegenberger, 1993; Hoffman et al., 2007; Hoffman and Schrag, 2002; James et al., 2001; Kennedy, 1996; Lorentz et al., 2004; MacDonald et al., 2009; Okubo et al., 2018; Peryt et al., 1990; Pruss et al., 2008; Saylor, 1998; Vieira et al., 2015). This conspicuous connection between the Neoproterozoic crystal fan development and glaciation might be a result of increased continental weathering following the deglaciation, during which CO_2 in the atmosphere would be substantially consumed and transferred into the ocean as carbonate ions. A subsequent rise in alkalinity likely have led to carbonate oversaturation and favored the growth of crystal fans. From another perspective, Bergmann et al (2013) discussed the effect of organic matter delivery and microbial respiration on the precipitation of two distinct ACF from the Paleoproterozoic and the Neoproterozoic. It appears that, although not all crystal fans represent a single set of depositional environments, the predominance of anaerobic respiration and slow delivery of organic matter into the water - sediment interface are favorable conditions in the two Proterozoic circumstances.

ACF may have occurred throughout the Mesoproterozoic, however, the few known occurrences from this period might be due to sampling bias (Fig. 13A). Most of them are restricted to carbonate formed in peritidal environments (Bergmann et al., 2013), including the Jixian, Billyakh and Dismal Lake groups in China, Siberia and Canada, respectively (Xiao et al., 1997; Bartley et al., 2000; Seong-Joo and Golubic, 2000; Kah et al., 2006; Tang et al., 2017). Occurrences of ACF have also been reported in Archean and Paleoproterozoic successions (Fig. 13A) (e.g., Allwood et al., 2009; Bergmann et al., 2013; Grotzinger, 1989; Grotzinger and James, 2000; Grotzinger and Reed, 1983; Hofmann et al., 2004; Hofmann and Jackson, 1987; Kah and Knoll, 1996; Kusky and Hudleston, 1999; Sami and James, 1996; Sumner and Grotzinger, 2004, 1996; Winefield, 2000), with the oldest record traced back to the 3.35 Ga Strelley Pool Formation in Western Australia (Grotzinger, 1989; Allwood et al., 2009). It is also noteworthy that there is an absence of the credible records of ACF from the initiation of the GOE until the end of the LJE, followed by the return of ACF in post - LJE strata (Fig. 13A). Although this could simply be the result of poor preservation of the fan - like fabric, the unprecedented large number of occurrences of ACF in Archean and Paleoproterozoic is more consistent with a primary sedimentary record, which corresponds to fundamental changes in marine environments and the global carbon cycle (Fig. 13).

5.5 A Post - LJE Expansion of the Dissolved Inorganic Carbon (DIC) Reservoir and Reappearance of ACF

The secular variations of oxygen level and the DIC reservoir have both been proposed as the driving force in the style of carbonate deposition in the long term (Bartley and Kah, 2004; Kump, 2008; Lyons et al., 2014). ACF formation at the Permian - Triassic boundary were thought to be facilitated by an increase in surface ocean alkalinity and the DIC reservoir following the expansion of the oxygen - minimum zone (Algeo et al., 2011; Hays et al., 2007; Riccardi et al., 2007). The decreasing abundance of seafloor precipitated crystal fans after the Paleoproterozoic has been linked to a decrease in the marine DIC reservoir and the removal of Fe^{2+} from seawater (Sumner and Grotzinger, 1996; Higgins et al., 2009). All of these hinted at a close link between the appearance of ACF and a decrease in oxygen level and an increase of the DIC reservoir. It is interesting to note that the occurrence of the ACF within the Huaiyincun Formation postdates the decline of $\delta^{13}C_{carb}$ at the termination of the Paleoproterozoic LJE (from > + 5‰ to ~ 0‰) (Fig. 2) (She et al., 2016; Ouyang et al., 2020). In addition, post - LJE ACF have also been reported from the coeval Belcher Group and Bear Creek Group in northern Canada, Libby Creek Group in western US (Hofmann and Jackson, 1987; Bekker and Eriksson, 2003; Bergmann et al., 2013) and late Paleoproterozoic successions in central India and northern Australia (Winefield and Creek, 2000; Sharma and Shukla, 2019). These likely indicate the onset of organic matter oxidation because the latter would not only produce a negative $\delta^{13}C_{carb}$ anomaly, but also consume O_2 in seawater, therefore creating a suitable environment for the formation of ACF.

In addition to the secular changes in the depositional styles of carbonate, short - term variability in C isotope composition of the seawater is also a function of the oceanic DIC reservoir size (Bartley and Kah, 2004; Hotinski et al., 2004). The negative C isotope excursion recorded in the Huaiyincun carbonates corresponds well to the decrease of $\delta^{13}C_{carb}$ values in other post - LJE successions (Ouyang et al., 2020). Although its origin is still being debated, this negative carbon isotopic excursion likely has resulted from a non - steady - state carbon cycle. Elevated input of ^{13}C - depleted carbon from buried organic matter would have altered the seawater C isotopic composition and led to the expansion of the DIC reservoir. To keep the oceans from freezing against the reduced solar luminosity, Kasting (1993) estimated that the atmospheric CO_2 at ca.2.0 Ga might have reached very high levels of up to 1000 times the present level. Assuming that the oceanic Ca^{2+} concentration at ca. 2.0 Ga was the same as the present level, the DIC reservoir at that time would have been at least five times greater than the present one (Hotinski et al., 2004). Intermittent upwellings of a small DIC reservoir would have altered the C isotopic composition of the seafloor carbonate precipitate (Winefield, 2000). However, $\delta^{13}C_{carb}$ values of the Huaiyincun crystal fans are almost identical to those of the surrounding matrix (Fig. 11A) and show no signal of heterogeneity. This could be attributed to a weak biological pump, or a large DIC reservoir in the post - GOE ocean, either of which could lead to a significant $\delta^{13}C$ gradient (Hotinski et al., 2004). With decreased oxygen levels and an expanded DIC reservoir in the post - LJE ocean, upwelling of deep, oxygen - poor seawater on the Dongye platform readily set up the local conditions for the formation of the Huaiyincun ACF.

In summary, we propose that the increasing occurrences of ACF after the LJE could have been intimately linked to the increase of the seawater DIC concentration and the shallowed Fe - chemocline. Extensive oxidation of organic matter as suggested by the slightly younger negative $\delta^{13}C$ excursion (Kump et al., 2011; Ouyang et al., 2020) might have led to the global expansion of the oceanic DIC reservoir. At the same time, consumption of O_2 during the oxidation of organic matter could have led to an upward expansion of deep ferruginous water, which in turn changed the global depositional style of post - LJE carbonates.

6. CONCLUSIONS

The occurrence of stromatolites, oolites and storm - related structures in the lower Huaiyincun pink dolostones documents a sunlit, subtidal environment with intermittent high - energy events. Temporal variations in stromatolite morphologies and ooids characterize frequent fluctuations of sea level. Occurrences of aragonite crystal fans (ACF) correspond to the deepening of seawater which led to the drowning of an earlier carbonate platform and the eventual disappearance of stromatolites.

The bedding - parallel distribution of the Huaiyincun ACF and their hexagonal cross-sections and square terminations, as well as homogeneous, near - zero $\delta^{13}C_{carb}$ values that are indistinguishable from that of the host dolostones, indicate that the ACF precipitated directly on the seafloor from post - LJE seawater. The common association of iron minerals with the ACF supports that the reduced iron might have acted as an inhibitor to micrite precipitation, therefore indirectly promoted the growth of the ACF. In the Huaiyincun environment, upwelling of anoxic, alkaline deep waters during the transgression likely have delivered alkalinity to the shallow seawater, also promoting the precipitation of aragonite fans on the seafloor.

Our literature survey reveals an absence of ACF during the GOE in contrast to frequent occurrences of ACF in Archean strata, which is attributed to the rise of O_2 in the paleo - ocean. This is followed by a remarkable, global reappearance of ACF recorded in post - LJE successions. The temporary distribution of ACF and their geological context, as exemplified in the Huaiyincun Formation, strongly suggest that sufficient supply of alkalinity, Fe^{2+} and carbonate supersaturation are key factors in facilitating ACF formation. An expansion of the DIC reservoir and ferruginous deep waters after the LJE are responsible for the reappearance of ACF on the late Paleoproterozoic seafloor.

ACKNOWLEDGEMENTS

This work was supported by the Strategic Priority Research Program of Chinese Academy of Sciences (grant No. XDB26020102) and National Natural Science Foundation of China (grant No. 42172337, 42130208, and 41272038), the 111 project of China (grant # BP0820004) and the State Key Laboratory of Biogeology and Environmental Geology, China University of Geosciences (GBL12101). G.O. thanks Fabin Pan for assistance in electron microprobe analysis, Yaguan Zhang for helpful discussion, and Dongdong Li, Yongshun Yu and Lisha

Yang for their helps in field work. Constructive reviews by Julie Bartley greatly improved this manuscript.

REFERENCES

Algeo, T. J., Kuwahara, K., Sano, H., Bates, S., Lyons, T., Elswick, E., Hinnov , L., Ellwood, B., Moser, J. and Maynard, J. B., 2011, Spatial variation in sediment fluxes, redox conditions, and productivity in the Permian-Triassic Panthalassic Ocean: Palaeogeography. Palaeoclimatology. Palaeoecology, v. 308, p, 65–83, https://doi.org/10.1016/j.palaeo.2010.07.007.

Allwood, A. C., Grotzinger, J. P., Knoll, A. H., Burch, I. W., Anderson, M. S., Coleman, M. L. and Kanik, I., 2009, Controls on development and diversity of Early Archean stromatolites: Proceedings of the National Academy of Sciences of the United States of America., v. 106, p, 9548–9555, https://doi.org/10.1073/pnas.0903323106.

Allwood, A. C., Walter, M. R., Kamber, B. S., Marshall, C. P. and Burch, I. W., 2006, Stromatolite reef from the Early Archaean era of Australia: Nature, v. 441, p, 714–718, https://doi.org/10.1038/nature04764.

Alvarenga, C., Santos, R. V., Vieira, L. C., Lima, B., Mancini, L. H., 2014, Meso-Neoproterozoic isotope stratigraphy on carbonates platforms in the Brasilia belt of Brazil: Precambrian Research, v. 251, p. 164–180, https://doi.org/10.1016/j.precamres.2014.06.011.

Andres, M. S. and Reid, R. P., 2006, Growth morphologies of modern marine stromatolites: A case study from Highborne Cay, Bahamas: Sedimentary. Geology, v. 185, p, 319–328, https://doi.org/10.1016/j.sedgeo.2005.12.020.

Bai, J., 1986, The Early Precambrian Geology of Wutaishan [in Chinese with English Abstract]: Tianjin, China, Tianjin Science and Technology Press.

Bartley, J. K. and Kah, L. C., 2004, Marine carbon reservoir, C_{org}-C_{carb} coupling, and the evolution of the Proterozoic carbon cycle: Geology, v. 32, p, 129–132, https://doi.org/10.1130/G19939.1.

Bartley, J. K., Knoll, A. H., Grotzinger, J. P. and Sergeev, V. N., 2000, Lithification and fabric genesis in precipitated stromatolites and associated peritidal carbonates, Mesoproterozoic Billyakh Group, Siberia, in: Grotzinger, J.P., James, N.P. (Eds.), Carbonate Sedimentation and Diagenesis in the Evolving Precambrian World, SEPM (Society of Economic Palaeontologists and Mineralogists, Tulsa) Special Publication v. 67, p, 59-73.

Bekker, A. and Eriksson, K. A., 2003, A Paleoproterozoic drowned carbonate platform on the southeastern margin of the Wyoming Craton: A record of the Kenorland breakup: Precambrian Res., v. 120, p. 327–364.

Bekker, A. and Holland, H. D., 2012, Oxygen overshoot and recovery during the early Paleoproterozoic: Earth Planet. Sci. Lett., v. 317–318, p, 295–304.

Bekker, A., Holland, H. D., Wang, P. L., Rumble, D., Stein, H. J., Hannah, J. L., Coetzee, L. L. and Beukes, N. J., 2004, Dating the rise of atmospheric oxygen: Nature, v. 427, p, 117–120.

Bekker, A., Holmden, C., Beukes, N. J., Kenig, F., Eglingtone, B., and Patterson, W. P., 2008, Fractionation between inorganic and organic carbon during the Lomagundi (2.22-2.1 Ga) carbon isotope excursion: Earth Planet. Sci. Lett., v. 271, p, 278–291.

Bekker, A., Karhu, J. A. and Kaufman, A. J., 2006, Carbon isotope record for the onset of the Lomagundi carbon isotope excursion in the Great Lakes area, North America: Precambrian Res., v. 148, p, 145–180.

Bergmann, K. D., Grotzinger, J. P. and Fischer, W. W., 2013, Biological influences on seafloor carbonate precipitation: Palaios, v. 28, p, 99–115.

Caird, R. A., Pufahl, P. K., Hiatt, E. E., Abram, M. B., Rocha, A. J. D. and Kyser, T. K., 2017, Ediacaran stromatolites and intertidal phosphorite of the Salitre Formation, Brazil: Phosphogenesis during the Neoproterozoic Oxygenation Event: Sediment. Geol., v. 350, p, 55–71.

Cantine, M. D., Knoll, A. H. and Bergmann, K. D., 2020, Carbonates before skeletons: A database approach: Earth-Science Rev., v. 20, p, 103065.

Chen, Y. J., Chen, W. Y., Li, Q. G., Santosh, M. and Li, J. R., 2019, Discovery of the Huronian Glaciation Event in China: Evidence from glacigenic diamictites in the Hutuo Group in Wutai Shan: Precambrian Res., v. 320, p, 1–12.

Chen, Z. Q., Chen, J., Tong, J. and Fraiser, M. L., 2010, Marine ecosystem changes from the latest Permian to Middle Triassic in Qingyan area, Guizhou, Southwest China: J. Earth Sci., v. 21, p, 125–129.

Clough, J. G. and Goldhammer, R. K., 2000, Evolution of the Neoproterozoic Katakturuk dolomite ramp complex, northeastern Brooks Range, Alaska. In: Grotzinger, J.P., James, N.P. (Eds.), Carbonate Sedimentation and Diagenesis in the Evolving Precambrian World, SEPM (Society of Economic Palaeontologists and Mineralogists, Tulsa) Special Publication v. 67, p, 209-241.

Coffey, J. M., Flannery, D. T., Walter, M. R. and George, S. C., 2013, Sedimentology, stratigraphy and geochemistry of a stromatolite biofacies in the 2.72Ga Tumbiana Formation, Fortescue Group, Western Australia: Precambrian Res., v. 236, p, 282–296.

Corsetti, F. A., Kidder, D. L. and Marenco, P. J., 2006, Trends in oolite dolomitization across the Neoproterozoic-Cambrian boundary: a case study from Death Valley, California: Sediment. Geol., v. 191, p, 135–150.

Cui, H., Xiao, S., Cai, Y., Peek, S., Plummer, R. E. and Kaufman, A. J., 2019, Sedimentology and chemostratigraphy of the terminal Ediacaran Dengying Formation at the Gaojiashan section, South China: Geol. Mag., v. 156, p, 1924–1948.

Dott, R. H. and Bourgeois, J., 1982, Hummocky stratification: significance of its variable bedding sequences: Geol. Soc. Am. Bull., v. 93, p, 663–680.

Du, L., Yang, C., Guo, J., Wang, W., Ren, L., Wan, Y. and Geng, Y., 2010, The age of the base of the Paleoproterozoic Hutuo Group in the Wutai Mountains area, North China Craton: SHRIMP zircon U-Pb dating of basaltic andesite: Chinese Sci. Bull., v. 55, p, 1782–1789.

Du, L., Yang C., Wyman, D. A., Nutman, A. P., Zhao, L., Lu, Z., Song, H., Geng, Y. and Ren, L., 2017, Zircon U-Pb ages and Lu-Hf isotope compositions from clastic rocks in the Hutuo Group: Further constraints on Paleoproterozoic tectonic evolution of the Trans-North China Orogen: Precambrian Res., v. 303, p, 291–314.

Feng, D., Chen, D., Peckmann, J. and Bohrmann, G., 2010, Authigenic carbonates from methane seeps of the northern Congo fan: Microbial formation mechanism: Mar. Pet. Geol., v. 27, p, 748–756.

Font, E., Nédélec, A., Trindade, R. I. F., Macouin, M. and Charrière, A., 2006, Chemostratigraphy of the Neoproterozoic Mirassol d'Oeste cap dolostones (Mato Grosso, Brazil): An alternative model for Marinoan cap dolostone formation: Earth Planet. Sci. Lett., v. 250, p, 89–103.

Friesenbichler, E., Richoz, S., Baud, A., Krystyn, L., Sahakyan, L., Vardanyan, S., Peckmann, J., Reitner, J. and Heindel, K., 2018, Sponge-microbial build-ups from the lowermost Triassic Chanakhchi section in southern Armenia: Microfacies and stable carbon isotopes: Palaeogeogr. Palaeoclimatol. Palaeoecol., v. 490, p, 653–672.

Galimov, E. M., Kuznetsova, N. G. and Prokhorov, V. S., 1968, On the problem of the Earth's ancient atmosphere composition in connection with results of isotope analysis of carbon from the Precambrian carbonates: Geochemistry, v. 11, p, 1376–1381 (in Russian).

Grammer, G. M., Crescini, C. M., Mcneill, D. F. and Taylor, L. H., 1999, Quantifying rates of syndepositional marine cementation in deeper platform environments-new insight into a fundamental process: J. Sediment. Res., v. 69, p, 202–207.

Greene, S. E., Bottjer, D. J., Corsetti, F. A., Berelson, W. M., Zonneveld, J. P., 2012, A subseafloor carbonate factory across the Triassic-Jurassic transition: Geology, v. 40, p, 1043–1046.

Grotzinger, J. P., 1989, Facies and evolution of Precambrian carbonate depositional systems: emergence of the modern platform archetype. In: Crevello, P. D., Wilson, J. L., Sarg, J. F., Read, J. F. (Eds.), Controls on Carbonate Platform and Basin Development: Soc. Econ. Paleont. Mineral, 79-106.

Grotzinger, J. P. and James, N. P., 2000, Precambrian carbonates: evolution of understanding. In: Grotzinger, J.P., James, N.P. (Eds.), Carbonate Sedimentation and Diagenesis in the Evolving Precambrian World, SEPM (Society of Economic Palaeontologists and Mineralogists, Tulsa) Special Publication v. 67, p, 3-20.

Grotzinger, J. P. and Knoll, A. H., 1995, Anomalous carbonate precipitates; is the Precambrian the key to the Permian: Palaios, v. 10, p, 578–596.

Grotzinger, J. P. and Reed, J. F., 1983, Evidence for primary aragonite precipitation, lower Proterozoic (1.9 Ga) Rocknest dolomite, Wopmay orogen, northwest Canada: Geology, v. 11, p, 710–713.

Hays, L. E., Beatty, T., Henderson, C. M., Love, G. D. and Summons, R. E., 2007, Evidence for photic zone euxinia through the end-Permian mass extinction in the Panthalassic Ocean (Peace River Basin, Western Canada): Palaeoworld, v. 16, p, 39–50.

Hegenberger, W., 1993, Stratigraphy and sedimentology of the Late Precambrian Witvlei and Nama Groups, east of Windhoek: Geological Survey of Namibia, Ministry of Mines and Energy, 17, 82p.

Heindel, K., Foster, W. J., Richoz, S., Birgel, D., Roden, V. J., Baud, A., Brandner, R., Krystyn, L., Mohtat, T., Koşun, E., Twitchett, R. J., Reitner, J. and Peckmann, J., 2018, The formation of microbial-metazoan bioherms and biostromes following the latest Permian mass extinction: Gondwana Res., v. 61, p, 187–202.

Heindel, K., Richoz, S., Birgel, D., Brandner, R., Klügel, A., Krystyn, L., Baud, A., Horacek, M., Mohtat, T. and Peckmann, J., 2015, Biogeochemical formation of calyx-shaped carbonate crystal fans in the subsurface of the Early Triassic seafloor: Gondwana Res., v. 27, p, 840–861.

Hennessy, J. and Knauth, L. P., 1985, Isotopic variations in dolomite concretions from the Monterey Formation, California: J. Sediment. Res., v. 55, p, 120–130.

Heydari, E., Hassanzadeh, J., Wade, W. J. and Ghazi, A. M., 2003, Permian-Triassic boundary interval in the Abadeh section of Iran with implications for mass extinction: Part 1 – Sedimentology: Palaeogeogr. Palaeoclimatol. Palaeoecol., v. 193, p, 405–423.

Higgins, J. A., Fischer, W. W. and Schrag, D. P., 2009, Oxygenation of the ocean and sediments: Consequences for the seafloor carbonate factory: Earth Planet. Sci. Lett., v. 284, p, 25–33.

Hoffman, P. F., Halverson, G. P., Domack, E. W., Husson, J. M., Higgins, J. A. and Schrag, D. P., 2007, Are basal Ediacaran (635 Ma) post-glacial "cap dolostones" diachronous: Earth Planet. Sci. Lett., v. 258, p, 114–131.

Hoffman, P. F. and Schrag, D. P., 2002, The snowball Earth hypothesis: Testing the limits of global change: Terra Nov., v. 14, p, 129–155.

Hofmann, A., Dirks, P. H. G. M. and Jelsma, H. A., 2004, Shallowing-upward carbonate cycles in the Belingwe Greenstone Belt, Zimbabwe: a record of Archean sea-level oscillations: J. Sediment. Res., v. 74, p, 64–81.

Hofmann, H. J. and Davidson, A., 1998, Paleoproterozoic stromatolites, Hurwitz Group, Quartzite Lake area, Northwest Territories, Canada: Can. J. Earth Sci., v. 35, p, 280–289.

Hofmann, H. J. and Jackson, G. D., 1987, Proterozoic ministromatolites with radial-fibrous fabric: Sedimentology, v. 34, p, 963–971.

Holland, H. D., 2002, Volcanic gases, black smokers, and the Great Oxidation Event: Geochim. Cosmochim. Acta, v. 66, p, 3811–3826.

Hotinski, R. M., Kump, L. R. and Arthur, M. A., 2004, The effectiveness of the Paleoproterozoic biological pump: A $\delta^{13}C$ gradient from platform carbonates of the Pethei Group (Great Slave Lake Supergroup, NWT): Bull. Geol. Soc. Am., v. 116, p, 539–554.

Irwin, H., Curtis, C. and Coleman, M., 1977, Isotopic evidence for source of diagenetic carbonates formed during burial of organic-rich sediments: Nature, v. 269, p, 209–213.

James, N. P., Narbonne, G. M. and Kyser, T. K., 2001, Late Neoproterozoic cap carbonates: Mackenzie mountains, northwestern Canada: Precipitation and global glacial meltdown: Can. J. Earth Sci., v. 38, p, 1229–1262.

Kah, L. C., Bartley, J. K., Frank, T. D. and Lyons, T. W., 2006, Reconstructing sea-level change from the internal architecture of stromatolite reefs: An example from the Mesoproterozoic Sulky Formation, Dismal Lakes Group, Arctic Canada: Can. J. Earth Sci., v. 43, p, 653–669.

Kah, L. C., Bartley, J. K. and Stagner, A. F., 2009, Reinterpreting a Proterozoic enigma: Conophyton-Jacutophyton stromatolites of the Mesoproterozoic Atar group, Mauritania: Int. Assoc. Sediment Spec. Pub., v. 41, p, 277–295.

Kah, L. C. and Knoll, A. H., 1996, Microbenthic distribution of Proterozoic tidal flats: environmental and taphonomic considerations: Geology, v. 24, p, 79–82.

Karhu, J. A. and Holland, H. D., 1996, Carbon isotopes and the rise of atmospheric oxygen: Geology, v. 24, p, 867–870.

Kasting, J. F., 1993, Earth' s Early Atmosphere: Science, v. 259, p, 920–926.

Kastner, M., 1999, Oceanic minerals: Their origin, nature of their environment, and significance: Proc. Natl. Acad. Sci. U. S. A., v. 96, p, 3380–3387.

Kennedy, M. J., 1996, Stratigraphy, sedimentology, and isotopic geochemistry of Australian Neoproterozoic postglacial cap dolostones: Deglaciation, $\delta^{13}C$ excursions, and carbonate precipitation: J. Sediment. Res., v. 66, p, 1050–1064.

Kershaw, S., Crasquin, S., Li, Y., Collin, P. Y., Forel, M. B., Mu, X., Baud, A., Wang, Y., Xie, S., Maurer, F. and Guo, L., 2012, Microbialites and global environmental change across the Permian-Triassic boundary: a synthesis: Geobiology, v. 10, p, 25–47.

Kershaw, S. and Guo, L. 2016, Beef and cone-in-cone calcite fibrous cements associated with the end-Permian and end-Triassic mass extinctions: Reassessment of processes of formation: J. Palaeogeogr., v. 5, p, 28–42.

Kershaw, S., Li, Y., Crasquin-Soleau, S., Feng, Q., Mu, X., Collin, P. Y., Reynolds, A. and Guo, L., 2007, Earliest Triassic microbialites in the South China block and other areas: controls on their growth and distribution: Facies, v. 53, p, 409–425.

Kiyokawa, S., Ito, T., Ikehara, M. and Kitajima, F., 2006, Middle Archean volcano-hydrothermal sequence: Bacterial microfossil-bearing 3.2 Ga Dixon Island Formation, coastal Pilbara terrane, Australia: Geo. Soc. Am. Bull., v. 118(1-2), p, 3-22.

Kranendonk, M., Webb, G. E. and Kamber, B. S. 2003, Geological and trace element evidence for a marine sedimentary environment of deposition and biogenicity of 3.45 Ga stromatolitic carbonates in the Pilbara Craton, and support for a reducing Archaean ocean: Geobiology, v. 1(2), p, 91-108.

Kump, L. R., 2008, The rise of atmospheric oxygen: Nature, v. 451, p, 277–278.

Kump, L. R., Junium, C., Arthur, M. A., Brasier, A., Fallick, A., Melezhik, V., Lepland, A., Črne, A. E. and Luo, G., 2010, Carbon and nitrogen cycling pursuant to the Great Oxidation Event: evidence from the Paleoproterozoic of Fennoscandia: J. Earth Sci., v. 21, p, 4-5.

Kump, L. R., Junium, C., Arthur, M. A., Brasier, A., Fallick, A., Melezhik, V., Lepland, A., Črne, A. E. and Luo, G., 2011, Isotopic evidence for massive oxidation of organic matter following the Great Oxidation Event: Science, v. 334, p, 1694–1696.

Kusky, T. M. and Hudleston, P. J., 1999, Growth and demise of an Archean carbonate platform, Steep Rock Lake, Ontario, Canada: Can. J. Earth Sci., v. 36, p, 565–584.

De Leeuw, N. H., 2002, Molecular dynamics simulations of the growth inhibiting effect of Fe^{2+}, Mg^{2+}, Cd^{2+}, and Sr^{2+} on calcite crystal growth: J. Phys. Chem. B, v. 106, p, 5241–5249.

Li, B., Yoon, H. I. and Park, B. K., 2000, Foraminiferal assemblages and $CaCO_3$ dissolution since the last deglaciation in the Maxwell Bay, King George Island, Antarctica: Mar. Geol., v. 169, p, 239-257.

Liu, C., Zhao, G., Sun, M., Zhang, J., He, Y., Yin, C., Wu, F. and Yang, J., 2011, U-Pb and Hf isotopic study of detrital zircons from the Hutuo group in the Trans-North China Orogen and tectonic implications: Gondwana Res., v. 20, p, 106–121.

Lu, S., Zhao, G., Wang, H. and Hao, G., 2008, Precambrian metamorphic basement and sedimentary cover of the North China Craton: A review: Precambrian Res., v. 160, p, 77–93.

Logan, B. W., Rezak, R. and Ginsburg, R. N., 1964, Classification and environmental significance of algal stromatolites: J. Geol., v. 72, p, 68–83.

Lorentz, N. J., Corsetti, F. A., Link, P. K. and Karl, P., 2004, Seafloor precipitates and C-isotope stratigraphy from the Neoproterozoic Scout Mountain Member of the Pocatello Formation, southeast Idaho: Implications for Neoproterozoic earth system behavior: Precambrian Res., v. 130, p, 57–70.

Luo, G., Ono, S., Beukes, N. J., Wang, D. T., Xie, S. and Summons, R. E., 2016, Rapid oxygenation of Earth's atmosphere 2.33 billion years ago: Sci. Adv., v. 2, e1600134.

Lyons, T. W., Reinhard, C. T. and Planavsky, N. J., 2014, The rise of oxygen in Earth's early ocean and atmosphere: Nature, v. 506, p, 307–315.

Macdonald, F. A., McClelland, W. C., Schrag, D. P. and MacDonald, W. P., 2009, Neoproterozoic glaciation on a carbonate platform margin in Arctic Alaska and the origin of the North Slope subterrane: Bull. Geol. Soc. Am., v. 121, p, 448–473.

Maloof, A. C., Halverson, G. P., Kirschvink, J. L., Schrag, D. P., Weiss, B. P., Hoffman, P. F., 2006, Combined paleomagnetic, isotopic, and stratigraphic evidence for true polar wander from the Neoproterozoic Akademikerbreen Group, Svalbard, Norway: Geol. Soc. Am. Bull., v. 118(9-10), p, 1099-1124.

Martin, A., Nisbet, E. G. and Bickle, M. J., 1980, Archaean stromatolites of the Belingwe greenstone belt, Zimbabwe (Rhodesia): Precambrian Res., v. 13, p, 337–362.

Martin, A. P., Condon, D. J., Prave, A. R. and Lepland, A., 2013, A review of temporal constraints for the Palaeoproterozoic large, positive carbonate carbon isotope excursion (the Lomagundi-Jatuli Event): Earth-Science Rev., v. 127, p, 242–261.

Museum, G., Biology, E., Baud, A., Richoz, S. and Pruss, S., 2007, The lower Triassic anachronistic carbonate facies in space and time: Glob. Planet. Change, v. 55, p, 81–89.

Nogueira, A. C. R., Claudio, R. C., Sial, A. N., Moura, C. A. V. and Fairchild, T. R., 2003, Soft-sediment deformation at the base of the Neoproterozoic Puga cap carbonate (southwestern Amazon craton, Brazil): Confirmation of rapid icehouse to greenhouse transition in snowball Earth: Geology, v. 31, p, 613–614.

Nutman, A. P., Bennett, V. C., Friend, C., Kranendonk, M. V., and Chivas, A. R., 2016, Rapid emergence of life shown by discovery of 3,700-million-year-old microbial structures. Nature v. 537, p, 535-538.

Okubo, J., Muscente, A. D., Luvizotto, G. L., Uhlein, G. J. and Warren, L. V., 2018, Phosphogenesis, aragonite fan formation and seafloor environments following the Marinoan glaciation: Precambrian Res., v. 311, p, 24–36.

Ossa Ossa, F., Eickmann, B., Hofmann, A., Planavsky, N. J., Asael, D., Pambo, F. and Bekker, A., 2018, Two-step deoxygenation at the end of the Paleoproterozoic Lomagundi Event: Earth Planet. Sci. Lett., v. 486, p, 70–83.

Ouyang G., She Z., Papineau D., Wang X., Luo G. and Li C., 2020, Dynamic carbon and sulfur cycling in the aftermath of the Lomagundi-Jatuli Event: Evidence from the Paleoproterozoic Hutuo Supergroup, North China Craton: Precambrian Res., v. 337, p, 105549.

Papineau, D., Mojzsis, S. J., Coath, C. D., Karhu, J. A., McKeegan, K. D., 2005a, Multiple sulfur isotopes of sulfides from sediments in the aftermath of Paleoproterozoic glaciations: Geochim. Cosmochim. Acta, v. 69, p, 5033–5060.

Papineau, D., Walker, J. J., Mojzsis, S. J. and Pace, N. R., 2005b, Composition and structure of microbial communities from stromatolites of Hamelin Pool in Shark Bay, Western Australia: Appl. Environ. Microbiol., v. 71, p, 4822-4832.

Papineau, D., Mojzsis, S.J. and Schmitt, A.K., 2007, Multiple sulfur isotopes from Paleoproterozoic Huronian interglacial sediments and the rise of atmospheric oxygen: Earth Planet. Sci. Lett., v. 255, p, 188–212.

Papineau, D., She, Z. and Dodd, M. S., 2017, Chemically-oscillating reactions during the diagenetic oxidation of organic matter and in the formation of granules in late Paleoproterozoic chert from Lake Superior: Chem. Geol., v, 470, p, 33–54.

Papineau, D., 2020, Chemically oscillating reactions in the formation of botryoidal malachite: Am. Mineral, v, 105, p, 447–454.

Papineau, D., Yin, J., Devine, K. G., Liu, D. and She, Z., 2021, Chemically oscillating reactions during the diagenetic formation of Ediacaran siliceous and carbonate botryoids: Minerals. v, 11, p, (1060) 1-30.

Peng, P., Zhai, M., Zhang, H. and Guo, J., 2005, Geochronological constraints on the Paleoproterozoic evolution of the north China craton: SHRIMP zircon ages of different types of mafic dikes: Int. Geol. Rev., v. 47, p, 492–508.

Peryt, T. M., Hoppe, A., Bechstädt, T., Köster, J., Pierre, C. and Richter, D. K., 1990, Late Proterozoic aragonitic cement crusts, Bambui Group, Minas Gerais, Brazil: Sedimentology, v. 37, p, 279–286.

Petroff, A. P., Sim, M. S., Maslov, A., Krupenin, M., Rothman, D. H., Bosak, T., Sub, M., Maslov, A., Krupenin, M., Rothman, D. H. and Bosak, T., 2010, Biophysical basis for the geometry of conical stromatolites: Proc. Natl. Acad. Sci. U. S. A., v. 107, p, 9956–9961.

Pierson, B. J., 1981, The control of cathodoluminescence in dolomite by iron and manganese: Sedimentology, v, 28(5), p, 601-610.

Pingitore, N. E., 1978, The behavior of Zn^{2+} during carbonate diagenesis: theory and applications: J. Sediment. Petrol., v, 48, p, 799–814.

Planavsky, N. J., Bekker, A., Hofmann, A., Owens, J. D. and Lyons, T. W., 2012, Sulfur record of rising and falling marine oxygen and sulfate levels during the Lomagundi event: Proc. Natl. Acad. Sci. U. S. A., v. 109, p, 18300–18305.

Poulton, S. W., Bekker, A., Cumming, V. M., Zerkle, A. L., Canfield, D. E. and Johnston, D. T., 2021, A 200-million-year delay in permanent atmospheric oxygenation: Nature, v. 592, p. 232–236.

Pruss, S. B., Corsetti, F. A. and Bottjer, D. J., 2005, The unusual sedimentary rock record of the Early Triassic: a case study from the southwestern United States: Palaeogeogr. Palaeoclimatol. Palaeoecol., v. 222, p, 33–52.

Pruss, S. B., Corsetti, F. A. and Fischer, W. W., 2008, Seafloor-precipitated carbonate fans in the Neoproterozoic Rainstorm Member, Johnnie Formation, Death Valley Region, USA: Sediment. Geol., v. 207, p, 34–40.

Qu, Y., Črne, A. E., Lepland, A. and van Zuilen, M. A., 2012, Methanotrophy in a Paleoproterozoic oil field ecosystem, Zaonega Formation, Karelia, Russia: Geobiology, v. 10, p, 467–478.

Qu, Y., Lepland, A., van Zuilen, M. A., Whitehouse, M., Črne, A. E. and Fallick, A. E., 2018, Sample-scale carbon isotopic variability and diverse biomass in the Paleoproterozoic Zaonega Formation, Russia: Precambrian Res., v. 315, p, 222–231.

Riccardi, A., Kump, L. R., Arthur, M. A. and Hondt, S. D., 2007, Carbon isotopic evidence for chemocline upward excursions during the end-Permian event: Palaeogeogr. Palaeoclimatol. Palaeoecol., v. 248, p, 73–81.

Richoz, S., Krystyn, L., Baud, A., Brandner, R., Horacek, M. and Mohtat-Aghai, P., 2010, Permian-Triassic boundary interval in the Middle East (Iran and N. Oman): Progressive environmental change from detailed carbonate carbon isotope marine curve and sedimentary evolution: J. Asian Earth Sci., v. 39, p, 236–253.

Mazzullo, S. J., 2000, Organogenic dolomitization in peritidal to deep-sea sediments: J. Sediment. Res., v. 70, p, 10–23.

Sami, T. T. and James, N. P., 1996, Synsedimentary cements as Paleoproterozoic platform building blocks, Pethei Group, northwestern Canada: J. Sediment. Res., v. 67, p, 614–615.

Saylor, B. Z., 1998, A composite reference section for terminal Proterozoic strata of Southern Namibia: J. Sediment. Res., v. 68, p, 1223–1235.

Schidlowski, M., Eichmann, R. and Junge, C. E., 1976, Carbon isotope geochemistry of the Precambrian Lomagundi carbonate province, Rhodesia: Geochim. Cosmochim. Acta, v. 40, p, 449–455.

Scott, C., Wing, B. A., Bekker, A., Planavsky, N. J., Medvedev, P., Bates, S. M., Yun, M. and Lyons, T. W., 2014, Pyrite multiple-sulfur isotope evidence for rapid expansion and contraction of the early Paleoproterozoic seawater sulfate reservoir: Earth Planet. Sci. Lett., v. 389, p, 95–104.

Seong-Joo, L. and Golubic, S., 2000, Biological and mineral components of an ancient stromatolite: Gaoyuzhuang Formation, Mesoproterozoic of China. In: Grotzinger, J.P., James, N.P. (Eds.), Carbonate Sedimentation and Diagenesis in the Evolving Precambrian World, SEPM (Society of Economic Palaeontologists and Mineralogists, Tulsa) Special Publication v.67, p, 91-102.

Sharma, M. and Shukla, B., 2019, Akinetes from Late Paleoproterozoic Salkhan limestone (>1600 Ma) of India: A proxy for understanding life in extreme conditions: Front. Microbiol., v. 10, p, 1-15.

She, Z., Yang, F., Liu, W., Xie, L., Wan, Y., Li, C. and Papineau, D., 2016, The termination and aftermath of the Lomagundi-Jatuli carbon isotope excursions in the Paleoproterozoic Hutuo Group, North China: J. Earth Sci., v. 27, p, 297–316.

Sommers, M. G., Awramik, S. M. and Woo, K. S., 2000, Evidence for initial calcite-aragonite composition of lower algal chert member ooids and stromatolites, Paleoproterozoic Gunflint formation, Ontario, Canada: Can. J. Earth Sci., v. 37, p, 1229–1243.

Soares, J. L., Nogueira, A., Santos, R., Sansjofre, P. and Truckenbrodt, W., 2020, Microfacies, diagenesis and hydrocarbon potential of the Neoproterozoic cap carbonate of the southern Amazon craton. Sediment. Geol., v. 406, p, 105720.

Song, H., Tong, J., Algeo, T. J., Song, H., Qiu, H., Zhu, Y., Tian, L., Bates, S., Lyons, T. W., Luo, G. and Kump, L. R., 2014, Early Triassic seawater sulfate drawdown: Geochim. Cosmochim. Acta, v. 128, p, 95–113.

Strasser, A., 1986, Ooids in Purbeck limestones (lowermost Cretaceous) of the Swiss and French Jura: Sedimentology, v. 33, p, 711–727.

Sumner, D. Y. and Grotzinger, J. P., 2004, Implications for Neoarchaean ocean chemistry from primary carbonate mineralogy of the Campbellrand-Malmani Platform, South Africa: Sedimentology, v. 51, p, 1273-1299.

Sumner, D. Y. and Grotzinger, J. P., 2000, Late Archean aragonite precipitation: petrography, facies associations, and environmental significance. In: Grotzinger, J.P., James, N.P. (Eds.), Carbonate Sedimentation and Diagenesis in the Evolving Precambrian World, SEPM (Society of Economic Palaeontologists and Mineralogists, Tulsa) Special Publication, v. 67, p, 123-144.

Sumner, D. Y. and Grotzinger, J. P., 1996, Were kinetics of Archean calcium carbonate precipitation related to oxygen concentration: Geology, v. 24, p, 119–122.

Tang, D. J., Shi, X. Y., Zhang, W. H., Liu, Y. and Wu, J. J., 2017, Mesoproterozoic herringbone calcite from North China Platform:Genesis and paleoenvironmental significance: J. Palaeogeogr. (Chinese Edition), v. 19(2), p, 227-240.

Thomazo, C., Buoncristiani, J. F., Vennin, E., Pellenard, P., Cocquerez, T., Mugnier, J. L. and Gérard, E., 2017, Geochemical processes leading to the precipitation of subglacial carbonate crusts at Bossons Glacier, Mont Blanc Massif (French Alps): Front. Earth Sci., v. 5, p, 1–16.

Turner, E. C., Narbonne, G. M. and James, N. P., 2000, Framework composition of early Neoproterozoic calcimicrobial reefs and associated microbialites, Mackenzie Mountains, NWT, Canada. In: Grotzinger, J.P., James, N.P. (Eds.), Carbonate Sedimentation and Diagenesis in the Evolving

Precambrian World, SEPM (Society of Economic Palaeontologists and Mineralogists, Tulsa) Special Publication v. 67, p, 179-205.

Turpin, M., Emmanuel, L., Reijmer, J. J. G. and Renard, M., 2011, Whiting-related sediment export along the Middle Miocene carbonate ramp of Great Bahama Bank. Int. J. Earth Sci. v. 100, p, 1875–1893.

Vanyo, J. P. and Awramik, S. M., 1985, Stromatolites and earth-sun-moon dynamics: Precambrian Res., v. 29, p, 121–142.

Viehmann, S., Reitner, J., Tepe, N., Hohl, S. V., Van Kranendonk, M., Hofmann, T., Koeberl, C. and Meister, P., 2020, Carbonates and cherts as archives of seawater chemistry and habitability on a carbonate platform 3.35 Ga ago: Insights from Sm/Nd dating and trace element analysis from the Strelley Pool Formation, Western Australia: Precambrian Res., v. 344, 105742.

Vieira, L. C., Nédélec, A., Fabre, S., Trindade, R. I. F. and De Almeida, R. P., 2015, Aragonite crystal fans in Neoproterozoic cap carbonates: A case study from Brazil and implications for the post-snowball earth coastal environment: J. Sediment. Res., v. 85, p, 285–300.

Walker, R. G., 1975, Generalized facies models for resedimented conglomerates of turbidite association: Geol. Soci. Am. Bull., v. 86, p, 737-748.

Walter, M. R., Buick, R. and Dunlop, J. S. R. 1980, Stromatolites 3,400-3,500 Myr old from the North Pole area, Western Australia: Nature, v, 284, p, 443-445.

Wan, Y., Liu, D., Wang, S., Yang, E., Wang, W., Dong, C., Zhou, H., Du, L., Yang, Y. and Diwu, C., 2011, ~ 2.7 Ga juvenile crust formation in the North China Craton (Taishan-Xintai area, western Shandong Province): further evidence of an understated event from U-Pb dating and Hf isotopic composition of zircon: Precambrian Res., v. 186, p, 169–180.

Wignall, P. B. and Twitchett, R. J., 1999, Unusual intraclastic limestones in Lower Triassic carbonates and their bearing on the aftermath of the end-Permian mass extinction. Sedimentology v. 46, p, 303–316.

Winefield, P. R. and Creek, B., 2000, Development of late Paleoproterozoic aragonitic seafloor cements in the McArthur Group, Northern Australia. In: Grotzinger, J.P., James, N.P. (Eds.), Carbonate Sedimentation and Diagenesis in the Evolving Precambrian World, SEPM (Society of Economic Palaeontologists and Mineralogists, Tulsa) Special Publication v. 67, p, 145–159.

Winguth, C. and Winguth, A. M. E., 2012, Simulating Permian-Triassic oceanic anoxia distribution: Implications for species extinction and recovery. Geology v. 40, p, 127–130.

Woods, A. D., 2014, Assessing Early Triassic paleoceanographic conditions via unusual sedimentary fabrics and features. Earth-Science Rev. v. 137, p, 6–18.

Woods, A. D. and Baud, A., 2008, Anachronistic facies from a drowned Lower Triassic carbonate platform: Lower member of the Alwa Formation (Ba'id Exotic), Oman Mountains. Sediment. Geol. v. 209, p, 1-14.

Woods, A. D., Bottjer, D. J. and Corsetti, F. A., 2007, Calcium carbonate seafloor precipitates from the outer shelf to slope facies of the Lower Triassic (Smithian-Spathian) Union Wash Formation, California, USA: Sedimentology and palaeobiologic significance. Palaeogeogr. Palaeoclimatol. Palaeoecol. v. 252, p, 281–290.

Woods, A. D., Bottjer, D. J., Mutti, M. and Morrison, J., 1999, Lower Triassic large sea-floor carbonate cements: Their origin and a mechanism for the prolonged biotic recovery from the end-Permian mass extinction. Geology v. 27, p, 645-648.

Xiao, S., Knoll, A. H., Kaufman, A. J., Yin, L. and Zhang, Y., 1997, Neoproterozoic fossils in Mesoproterozoic rocks? Chemostratigraphic resolution of a biostratigraphic conundrum from the North China Platform. Precambrian Res. v. 84, p, 197-220.

Zhai, M., Bian, A. and Zhao, T., 2000, The amalgamation of the supercontinent of North China Craton at the end of Neo-Archaean and its breakup during late Palaeoproterozoic and Meso-Proterozoic. Sci. China Ser. D Earth Sci. v. 43, p, 219-232.

Zhai, M., Zhu, X., Zhou, Y., Zhao, L. and Zhou, L., 2020, Journal of Asian Earth Sciences Continental crustal evolution and synchronous metallogeny through time in the North China Craton. J. Asian Earth Sci. v. 194, 104169.

Zhao, G., Wilde, S. A., Cawood, P. A. and Sun, M., 2001, Archean blocks and their boundaries in the North China Craton : lithological , geochemical , structural and P – T path constraints and tectonic evolution. Precambrian Res. v. 107, p, 45-73.

Zhao, G., Sun, M., Wilde, S. A. and Li, S., 2003, Assembly, Accretion and Breakup of the Paleo-Mesoproterozoic Columbia Supercontinent: Records in the North China Craton. Gondwana Res. v. 6, p, 417-434.

Zhao, G., Sun, M., Wilde, S. A. and Li S., 2005, Late Archean to Paleoproterozoic evolution of the North China Craton: key issues revisited. Precambrian Res. v. 136, p, 177-202.

FIGURE CAPTIONS

Figure 1. Geological maps. (A) Tectonic framework of the North China Craton showing the distribution of early Precambrian basement rocks (modified from Zhao et al, 2005). (B) Simplified geological map of the Wutai area (modified from Bai, 1986).

Figure 2. Generalized stratigraphic column of the Hutuo Supergroup (modified from Bai, 1986) and the Lower Huaiyincun Formation. Ar, Archean. Age data in the left column are from Wilde et al. (2004), Liu et al. (2011), Du et al. (2010, 2011) and Peng et al. (2017). $\delta^{13}C_{carb}$ data are from Ouyang et al. (2020).

Figure 3. Storm-related structures in the lower pink dolostone unit of the Huaiyincun Formation. (A) Unsorted centimeter-scale dolomitic intraclasts (white arrows). (B) Intraclasts (white arrows) parallel to sedimentary laminae. (C) Dolomitic intraclasts (white arrows) preserved within the stromatolite laminae. (D) Scour structure and dolomitic intraclasts. (E) Centimeter-scale graded dolostone bed (vertical arrow showing the upward fining trend). (F) Hummocky cross stratification at the top of the pink dolostone unit.

Figure 4. Stromatolites in the pink-dolostone unit of the Huaiyincun Formation. (A) Centimeter-sized coniform stromatolites showing gradual upward inclination of the axis (dashed line). (B) Coniform stromatolites (white arrows) occur as a lenticular body within the dolostone bed. (C) Wavy stromatolites with gently convex laminations. (D) Columnar stromatolites. (E) Wavy stromatolites overlying columnar stromatolites. (F) Wavy stromatolites underlying columnar stromatolites. (G) Bioherms composed of columnar and wavy stromatolites. (H) Disturbance of sediments between the columnar stromatolites (white dashed outlines) within the bioherm.

Figure 5. Oolites and intraclasts between two stromatolitic bioherm beds in the lower Huaiyincun Formation. (A) Outcrop photo of an oolite. The diameter of the coin is 25 mm. (B) An intraclastic bed. White arrows denote the intraclasts. (C-E) Transmitted light photomicrographs. (C) Millimeter-sized, irregular intraclasts composed of micritic dolomite. (D) Ooids with dark micritic nuclei (white arrows). (E) Radiating acicular crystals in the ooids interrupted by concentric laminae.

Figure 6. Outcrop photos of the stromatolitic bioherms and crystal fans (ACF). (A) The overall view of the ACF-bearing zone overlying the bioherms. Geologist in the photo is about 1.75 m in height. (B) Sketch of the panel (A) showing the distribution of crystal fans and columnar stromatolites in the bioherm. (C) Close-up of the ACF-bearing layers (white box). (D) ACF-bearing layers with flat bottom, layers with irregular upper and lower bounding surfaces can be observed. (E) Sketch of (D) highlighting clearly visible ACF and bounding surfaces of the layers. (F) Top view of the ACF. (G) Tilted and overturned crystal fans highlighted with sketches. (H) ACF-rich layers interbedded with hummocky cross - stratified (HCS) dolostone.

Figure 7. Plane-polarized light images of dolomitized ACF. (A) Oblique section of tightly clustered ACF, with micritic dolomite filling the inter-needle spaces. (B) Longitudinal sections of ACF crystals and dark, finer interstitial dolomite matrix. (C) Longitudinal section of the ACF showing square terminations of the crystal pseudomorphs. (D) Hexagonal cross sections of the ACF crystals. (E) Co-occurrence of millimeter -scale stromatolites and ACF.

Figure 8. SEM images and EDS maps of a dolomitized ACF. (A) Back scattered electron (BSE) image showing the trapped matrix along the ACF. (B-C) EDS elemental maps of Al and Si for panel A. (D-F) EDS maps of Al, Si and Fe for the outlined area in (A) showing disseminated clays in the dolomite matrix.

Figure 9. Mineral association for ACF and ooids. (A) Plane Polarized Light (PPL) image of the Raman scan area of the ACF. (B) PPL image of the ACF boundary. (C) Raman image of panel B showing the distribution of hematite and other minor phases within the matrix between the acicular crystal pseudomorphs. (D) PPL image of ooids. (E) PPL image of the ooid nucleus outlined in (D). (F) Raman image of panel E showing quartz and minor amounts of hematite and organic matter in the ooid nucleus. (G) Raman spectra of various minerals highlighted in the Raman images. Color coding of the mineral phases in (C) and (F): pink-clay mineral (Clay), green-dolomite (Dol), white-feldspar (Fsp), yellow-anatase (Ant), purple-hematite (Hem), blue-quartz (Qz), cyan-apatite (Ap), red-organic matter (OM).

Figure 10. Plane polarized light photomicrographs and corresponding cathodoluminescence images of the transverse (A, B) and longitudinal (C, D) sections of dolomitized ACF. The dolomitized ACF are dully-luminescent, whereas the surrounding matrix is luminescent.

Figure 11. C and O isotope data for an ACF-bearing slab. (A) Carbonate $\delta^{13}C$ (left) and $\delta^{18}O$ (right) values for dolomitized ACF (triangles) and dolomite matrix (circles) micro-drilled on the slab. The white scale bars are all 1 cm in length. (B-C) Cross plots of $\delta^{13}C_{carb}$ vs. $\delta^{18}O_{carb}$ (B) and Mg/Ca (molar ratio) vs. $\delta^{13}C_{carb}$ (C).

Figure 12. Cartoons showing a typical depositional cycle in the lower Huaiyincun Formation with an emphasis on the growth of stromatolites and ACF. (A–D) Evolution of stromatolite morphology from coniform to wavy, columnar and domal during the sea level fall. (E –G) Growth of ACF growth on domical bioherms (E, G), formation of ooids (F) and deposition of horizontally bedded dolostone (H) during the subsequent transgression.

Figure 13. Occurrences of ACF and glaciations in the geological history (A) and evolution of the carbon cycle (B) and Earth’s atmospheric oxygen (C) (B and C modified from Lyons et al., 2014). The dark grey bands in (A) represent unambiguous records of ACF reported in literature and in this study.

TABLE 1. OCCURRENCES OF ARAGONITE CRYSTAL FANS IN GEOLOGICAL HISTORY

Location	**Country**	**Age (Ma)**	**Reference**
Union Wash Formation	USA	Permian-Triassic Transition	Woods et al., 1999
Chanakhchi section, Karabaglyar Formation	Armenia	Permian-Triassic Transition	Friesenbichler et al., 2018
Kangan Formation	Iran	Permian-Triassic Transition	Heindel et al., 2018
Kuh e Dena section, Kangan Formation	Iran	Permian-Triassic Transition	Heindel et al., 2015
Alwa Formation	Oman	Permian-Triassic Transition	Woods and Baud, 2008
Baid section, Oman Mountain	Oman	Permian-Triassic Transition	Baud et al., 2007
Shareza Formation	Iran	Permian-Triassic Transition	
Çürük dag Formation	Turkey	Permian-Triassic Transition	Baud et al., 2005
Rainstorm Member of Johnnie Formation	U.S.A.	580 - 550	Pruss et al., 2008; Bergmann et al., 2013
Algal Dolostone Member, Dengying Formation	China	ca.635	Cui et al., 2019
Buschmannsklippe Formation	Namibia	Proterozoic–Cambrian boundary	Hegenberger, 1993; Saylor et al., 1998; Grotzinger and James et al., 2000
Hayhook Formation	Canada	Following Marinoan glaciation	James et al., 2001
Ravensthroat cap carbonate	Canada	Following Marinoan glaciation	Grotzinger and James et al., 2000
Katakturuk Dolomite	Arctic Alaska	Following Marinoan glaciation	Clough and Goldhammer, 2000; Macdonald et a., 2009
Guia Formation, Araras Group	Brazil	Following the Neoproterozoic Puga glaciation	Nogueira et al., 2003; Soares et al., 2020
Keilberg cap dolostone	Namibia	Following Marinoan glaciation	Hoffmann et al., 2007
Sete Lagoas Formation, Bambui Group	Brazil	Following Marinoan glaciation	Vieira et al., 2015; Okubo et al., 2018; Peryt et al., 1990
Upper Paranoá Group	Brazil	ca.635	Alvarenga et al., 2014
Hayhook Fm, Windermere Supergroup	Canada	ca.635	James et al., 2001; Hoffmann and Schrag, 2002

Grusdievbreen Formation, Akademikerbreen Group	Norway	ca.800	Maloof et al., 2006
Society Cliffs Formation, Bylot Supergroup	Canada	Late Mesoproterozoic	Kah and Knoll, 1996
Wumishan Formation, Jixian Group	China	Mesoproterozoic	Tang et al.,2011; Xiao et al., 1997
Longjianan Formation, Luonan Group	China	Mesoproterozoic	Xiao et al., 1997
Luoyukou Formation, Luoyu Group	China	Mesoproterozoic	Xiao et al., 1997
Sulky Formation, Dismal Lakes Group	Canada	ca.1300	Kah et al., 2006
Kotuikan Formation, Billyakh Group	Siberia	>1300	Bartly et al., 2000
Gaoyuzhuang Formation, Changcheng Group	China	1400	Seong-Joo and Golubic, 2000; Shi et al., 2010
Jaradag Fawn Limestone Formation	India	1600	Sharma and Shukla, 2019
Salkhan Limestone, Semri Group	India	>1600	Sharma and Shukla_2019
Rocknest Formation, Wopmay orogen	Canada	ca.1900	Grotzinger and Reed, 1983
Pethei Group	Canada	1880	Sami and James, 1996
Huaiyincun Formation, Hutuo Group	China	ca.1900	This study
Teena Formation of McArthur Group	Australia	1640	Winefield and Creek, 2000 Winefield, 2000
Mcleary Formation, Belcher Supergroup	Canada	1900	Hofmann and Jackson, 1987
Beechey Formation, Bear Creek Group	Canada	1970	Bergmann et al., 2013
Lower Algal Chert, Gunflint Formation	Canada	ca.2000	Sommers et al., 2000
Nash Fork Formation, Libby Greek Group	U.S.A.	ca.2062	Bekker and Eriksson, 2003
Campbellrand-Malmani Carbonate, Transvaal Supergroup	South Africa	2521	Sumner and Grotzinger, 2000; Grotzinger, 1989; Sumner and Grotzinger, 2004
Carawine Formation	Australia	2600	Sumner and Grotzinger, 2000
Huntsman Limestone	Zimbabwe	2600	Sumner and Grotzinger, 2000
Cheshire Formation Ngezi Group	Zimbabwe	2700	Sumner and Grotzinger, 2000; Hofmann et al., 2004
Steep Rock Group	Canada	2700	Sumner and Grotzinger, 2000; Kusky and Hudleston, 1999
Uchi Greenstone Belt	Canada	2930	Sumner and Grotzinger, 2000; Hofmann et al., 1985
Dixon Island Formation	Australia	3200	Kiyokawa et al., 2006
Strelley Pool Formation	Australia	3450	Grotzinger, 1989; Kranedonk et al., 2003; Allwood et al., 2009

TABLE 2. MAJOR OXIDE AND C-O ISOTOPE COMPOSITION OF DOLOMITE FROM THE POLISHED SLAB OF THE ARAGONITE CRYSTAL FAN BEARING SECTION IN THE HUAIYINCUN FORMATION

Spot No.	MgO (Wt%)	CaO (Wt%)	FeO (Wt%)	SiO_2 (Wt%)	Total (Wt%)	Mg (%)	Ca (%)	Fe (%)	Mg/Ca	$\delta^{13}C_{carb}$ (‰V-PDB)	$\delta^{18}O_{carb}$ (‰, V-PDB)
1	20.5	27.7	0.8	0.7	99.4	23.9	23.1	0.5	1.03	0.2	-6.3
2	19.4	26.7	0.8	9.5	106.7	21.5	21.1	0.5	1.02	0.1	-6.7
2r	19.0	25.0	0.7	12.9	108.1	22.9	19.5	0.4	1.18	*N.D.	*N.D.
3	20.9	29.6	0.5	0.2	99.4	24.3	24.5	0.3	0.99	0.1	-6.8
4	20.8	29.7	0.4	0.1	99.0	24.2	24.7	0.3	0.98	0.2	-6.7
5	19.9	28.4	0.6	1.3	99.7	23.3	23.7	0.4	0.98	0.2	-6.7
6	20.5	29.0	0.7	0.0	98.4	24.0	24.3	0.4	0.99	0.3	-6.4
7	20.6	29.0	0.7	0.1	98.7	24.1	24.2	0.4	1.00	0.2	-6.7
8	20.4	29.5	0.6	0.1	98.9	23.8	24.6	0.4	0.97	0.2	-6.5
9	20.3	29.2	0.6	0.1	98.5	23.8	24.4	0.4	0.97	0.2	-6.3
10	19.8	27.9	0.6	2.6	101.3	22.9	23.0	0.4	0.99	0.3	-6.4
11	20.7	29.0	0.5	0.2	98.8	24.1	24.2	0.3	1.00	0.2	-6.6
12	21.0	29.1	0.5	0.2	99.0	24.4	24.2	0.3	1.01	0.2	-6.4
13	20.4	28.6	0.6	0.9	99.0	23.8	23.8	0.4	1.00	0.3	-6.5
14	20.6	29.1	0.5	0.2	99.4	24.1	24.3	0.3	0.99	0.2	-6.6
15	20.4	29.2	0.6	0.0	98.4	23.9	23.1	0.5	1.03	0.2	-6.6

Note: Mg/Ca values are molar ratios.

*N.D. = not detected. ; VPDB—Vienna Pee Dee belemnite; carb—cabonate.

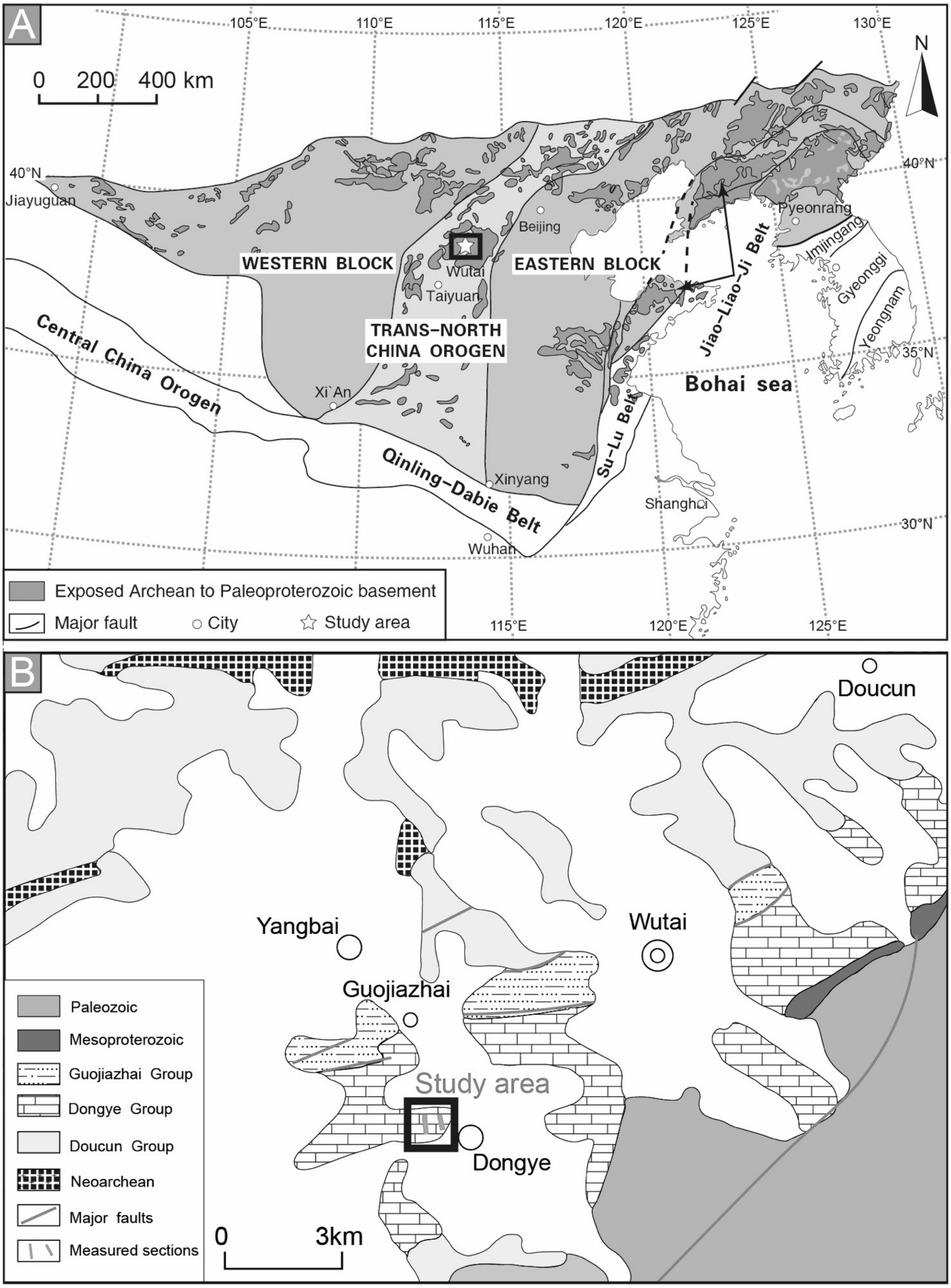

Fig. 1. Geological maps. (A) Tectonic framework of the North China Craton showing the distribution of early Precambrian basement rocks (modified from Zhao et al, 2005). (B) Simplified geological map of the Wutai area (modified from Bai, 1986).

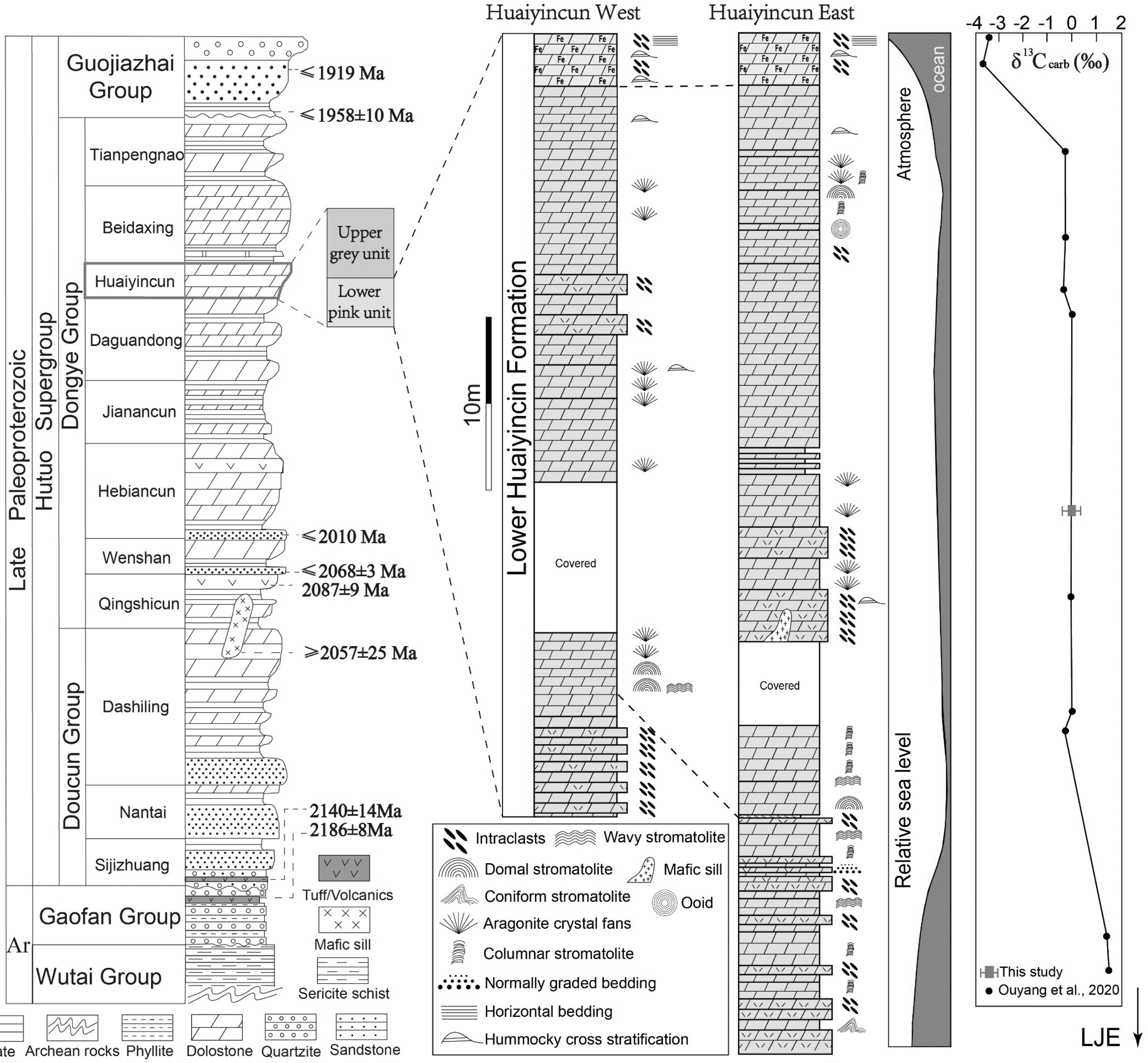

Fig. 2. Generalized stratigraphic column of the Hutuo Supergroup (modified from Bai, 1986) and the Lower Huaiyincun Formation. Ar, Archean. Age data in the left column are from Wilde et al. (2004), Liu et al. (2011), Du et al. (2010, 2011) and Peng et al. (2017). $\delta^{13}C_{carb}$ data are from Ouyang et al. (2020).

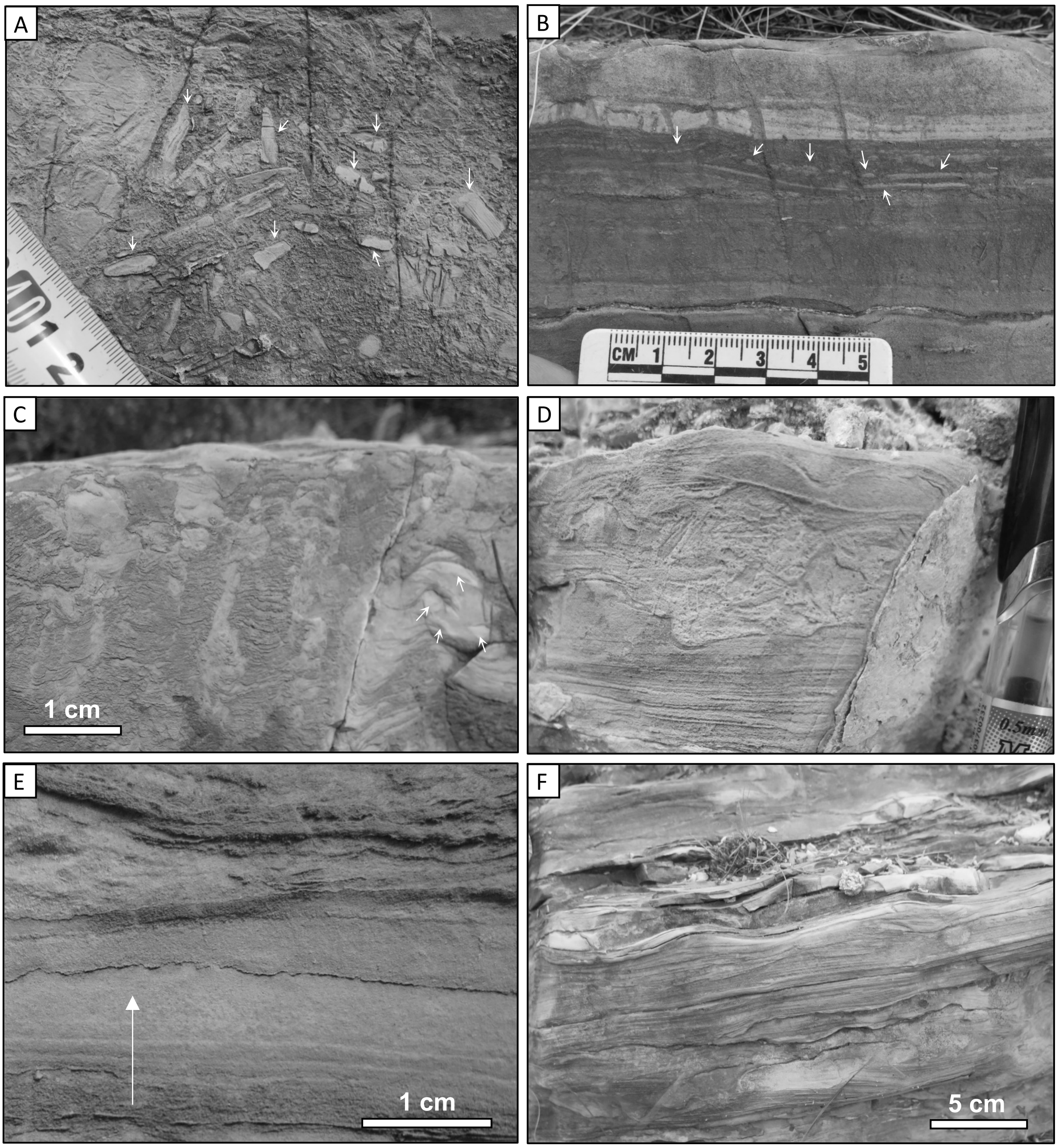

Fig. 3. Storm-related structures in the lower pink dolostone unit of the Huaiyincun Formation. (A) Unsorted centimeter-scale dolomitic intraclasts (white arrows). (B) Intraclasts (white arrows) parallel to sedimentary laminae. (C) Dolomitic intraclasts (white arrows) preserved within the stromatolite laminae. (D) Scour structure and dolomitic intraclasts. (E) Centimeter-scale graded dolostone bed (vertical arrow showing the upward fining trend). (F) Hummocky cross stratification at the top of the pink dolostone unit.

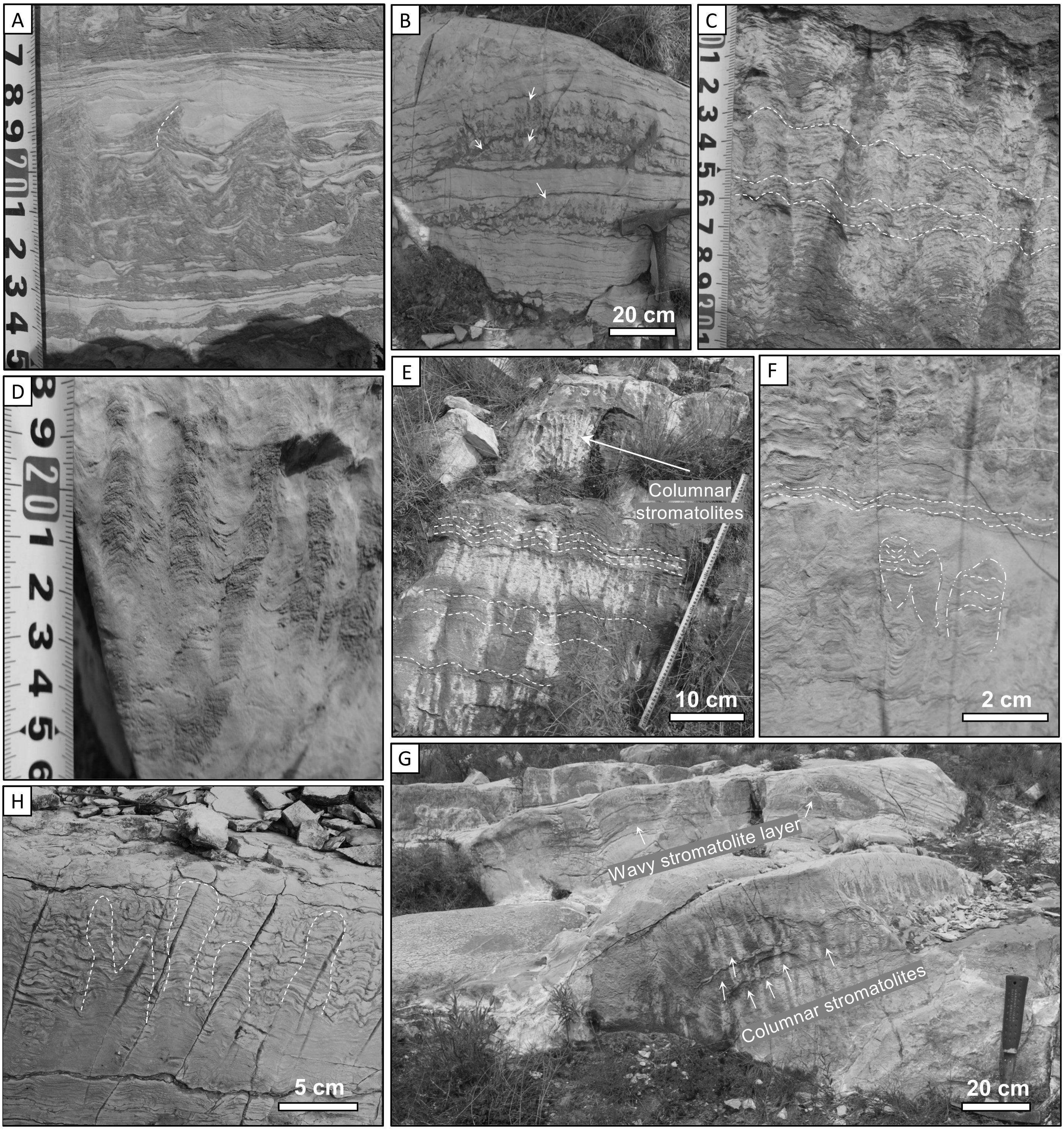

Fig. 4. Stromatolites in the pink-dolostone unit of the Huaiyincun Formation. (A) Centimeter-sized coniform stromatolites showing gradual upward inclination of the axis (dashed line). (B) Coniform stromatolites (white arrows) occur as a lenticular body within the dolostone bed. (C) Wavy stromatolites with gently convex laminations. (D) Columnar stromatolites. (E) Wavy stromatolites overlying columnar stromatolites. (F) Wavy stromatolites underlying columnar stromatolites. (G) Bioherms composed of columnar and wavy stromatolites. (H) Disturbance of sediments between the columnar stromatolites (white dashed outlines) within the bioherm.

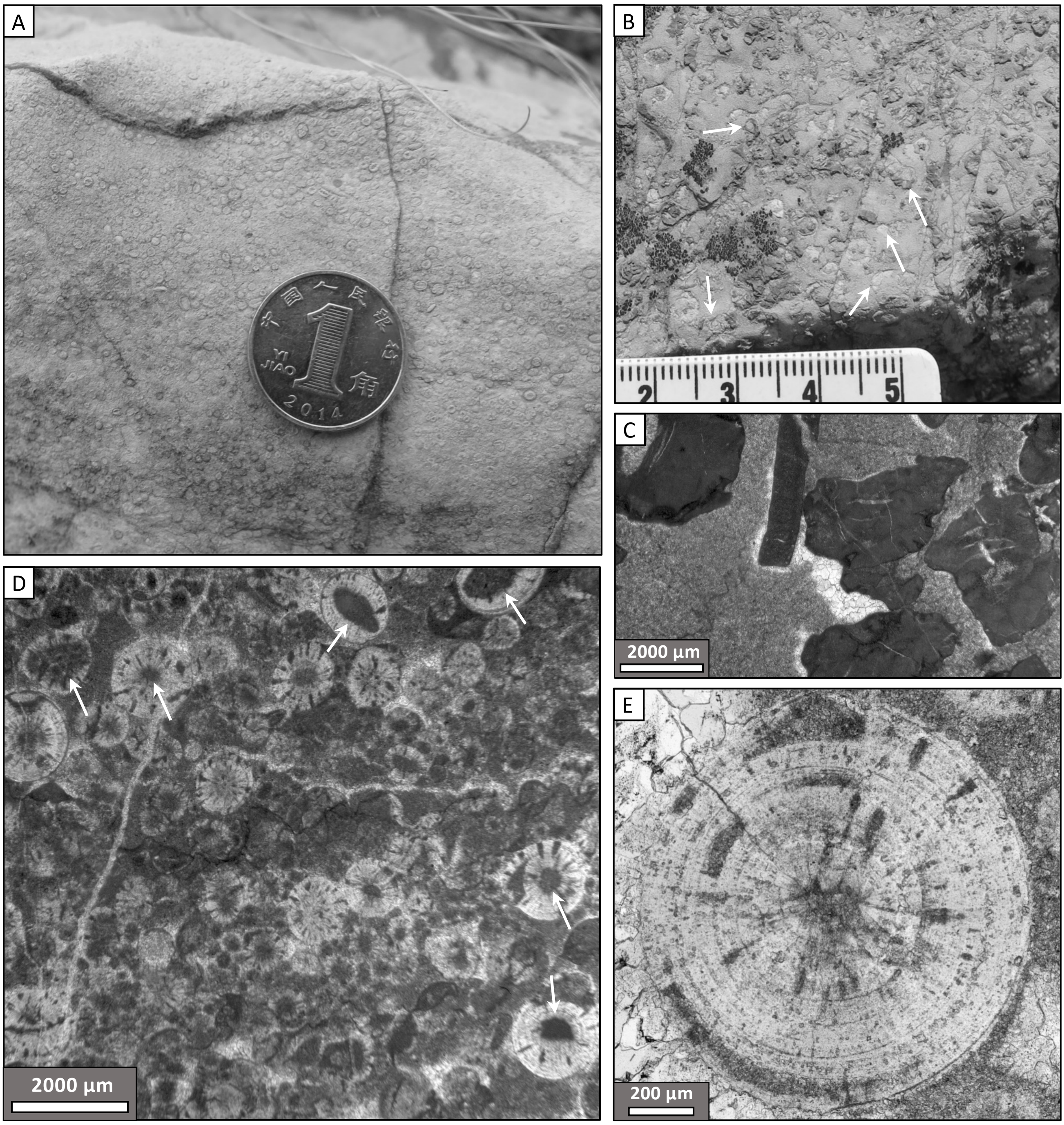

Fig. 5. Oolites and intraclasts between two stromatolitic bioherm beds in the lower Huaiyincun Formation. (A) Outcrop photo of an oolite. The diameter of the coin is 25 mm. (B) An intraclastic bed. White arrows denote the intraclasts. (C-E) Transmitted light photomicrographs. (C) Millimeter-sized, irregular intraclasts composed of micritic dolomite. (D) Ooids with dark micritic nuclei (white arrows). (E) Radiating acicular crystals in the ooids interrupted by concentric laminae.

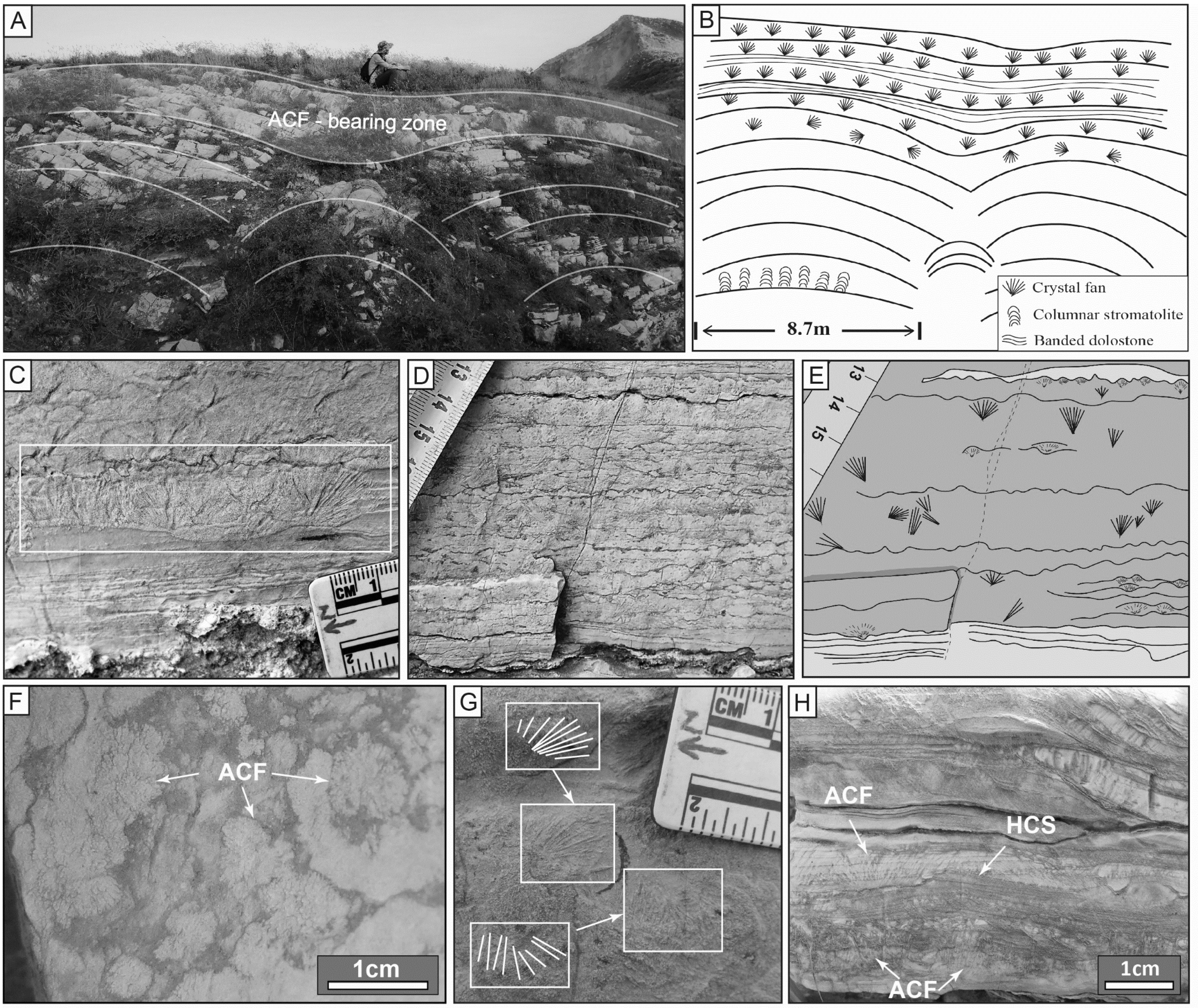

Fig. 6. Outcrop photos of the stromatolitic bioherms and crystal fans (ACF). (A) The overall view of the ACF-bearing zone overlying the bioherms. Geologist in the photo is about 1.75 m in height. (B) Sketch of panel (A) showing the distribution of crystal fans and columnar stromatolites in the bioherm. (C) Close-up of the ACF-bearing layers (white box). (D) ACF-bearing layers with flat bottom, layers with irregular upper and lower bounding surfaces can be observed. (E) Sketch of (D) highlighting clearly visible ACF and bounding surfaces of the layers. ACF-bearing layers were colored in brown, curves inside denote the upper / lower bounding surfaces. (F) Top view of ACF. (G) Tilted and overturned crystal fans highlighted with sketches. (H) ACF-rich layers interbedded with hummocky cross-stratified (HCS) dolostone.

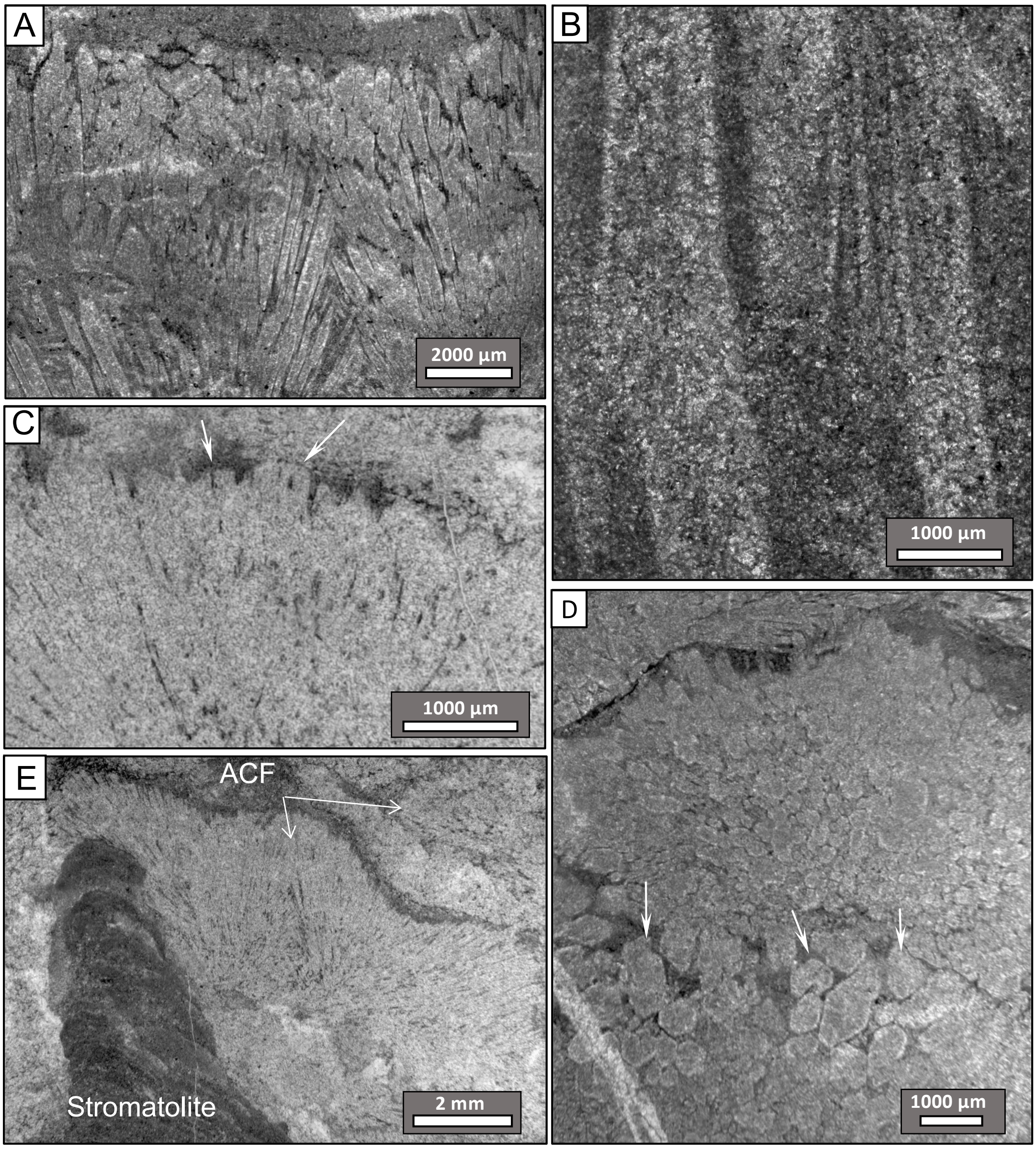

Fig. 7. Plane-polarized light images of dolomitized ACF. (A) Oblique section of tightly clustered ACF, with micritic dolomite filling the inter-needle spaces. (B) Longitudinal sections of ACF crystals and dark, finer interstitial dolomite matrix. (C) Longitudinal section of the ACF showing square terminations of the crystal pseudomorphs. (D) Hexagonal cross sections of the ACF crystals. (E) Co-occurrence of millimeter -scale stromatolites and ACF.

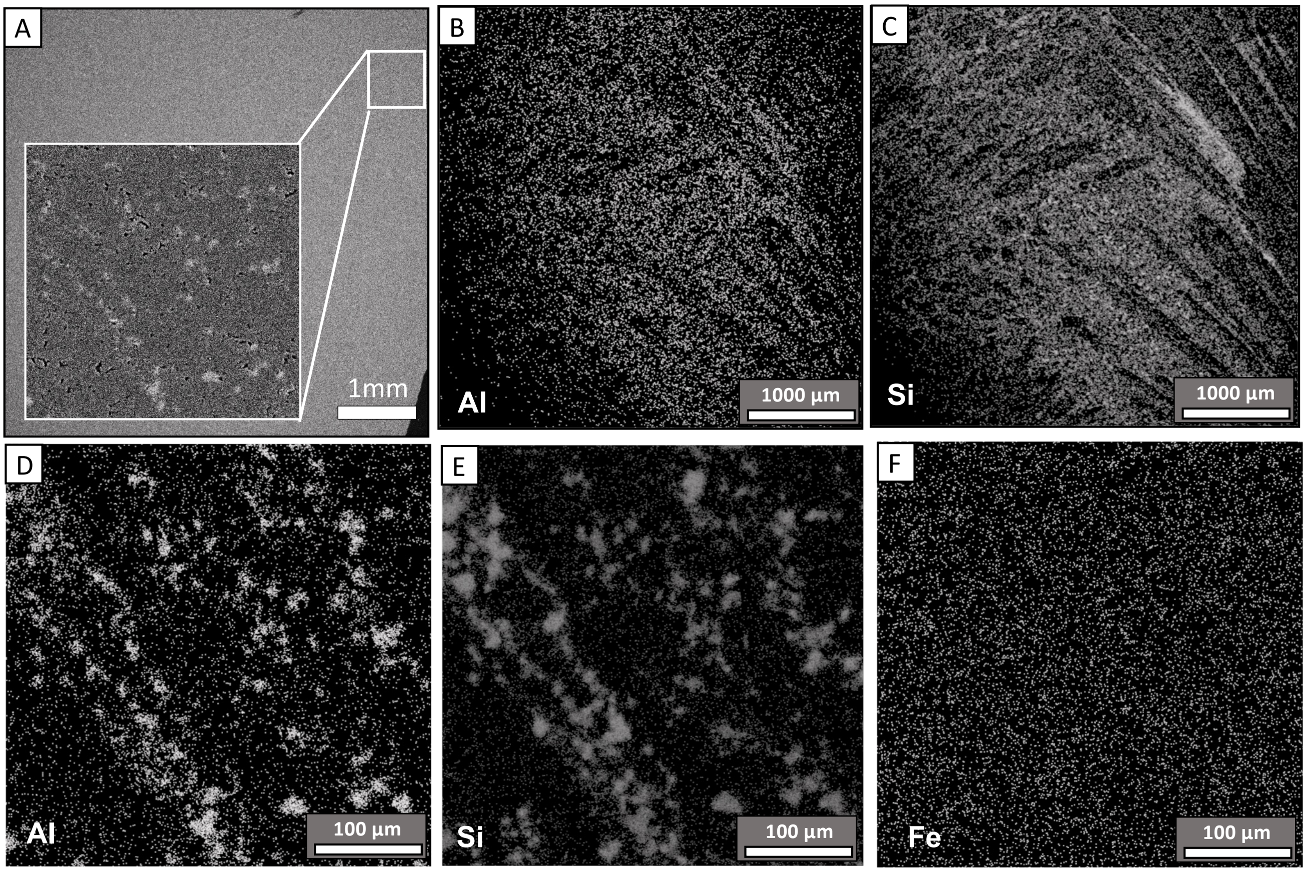

Fig. 8. SEM images and EDS maps of a dolomitized ACF. (A) Back scattered electron (BSE) image showing the trapped matrix along the ACF. (B-C) EDS elemental maps of Al and Si for panel A. (D-F) EDS maps of Al, Si and Fe for the outlined area in (A) showing disseminated clays in the dolomite matrix.

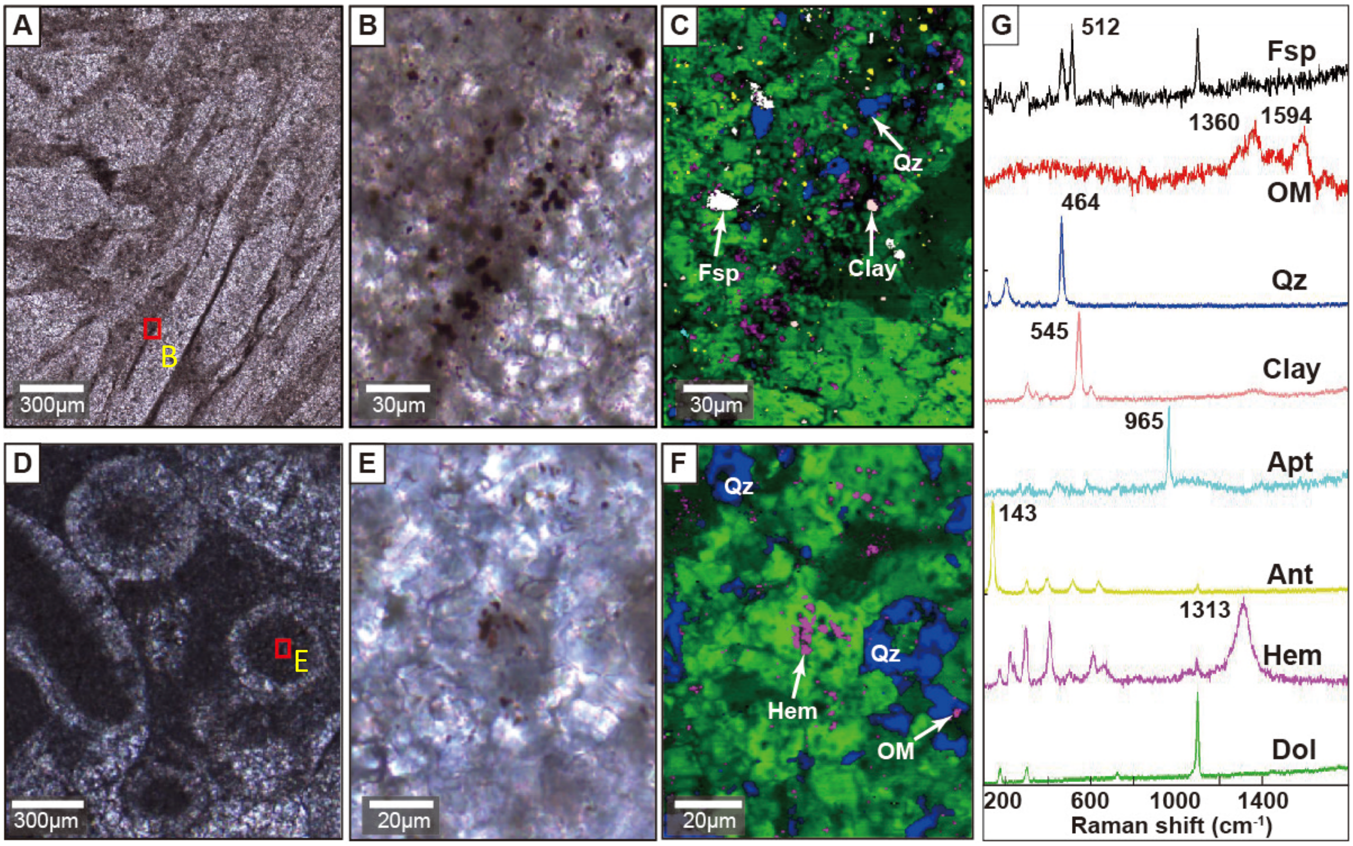

Fig. 9. Mineral association for ACF and ooids. (A) Plane Polarized Light (PPL) image of the Raman scan area of the ACF. (B) PPL image of the ACF boundary. (C) Raman image of panel B showing the distribution of hematite and other minor phases within the matrix between the acicular crystal pseudomorphs. (D) PPL image of ooids. (E) PPL image of the ooid nucleus outlined in (D). (F) Raman image of panel E showing quartz and minor amounts of hematite and organic matter in the ooid nucleus. (G) Raman spectra of various minerals highlighted in the Raman images. Color coding of the mineral phases in (C) and (F): pink-clay mineral (Clay), green-dolomite (Dol), white-feldspar (Fsp), yellow-anatase (Ant), purple-hematite (Hem), blue-quartz (Qz), cyan-apatite (Ap), red-organic matter (OM).

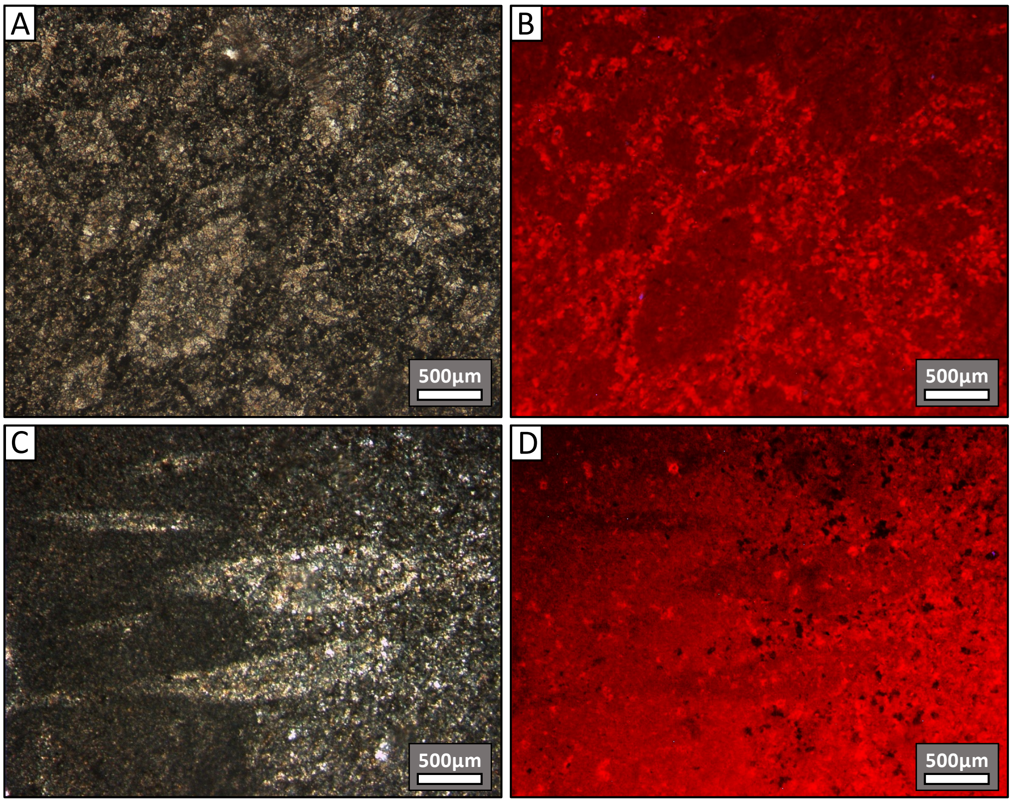

Fig. 10. Plane polarized light photomicrographs and corresponding cathodoluminescence images of the transverse (A, B) and longitudinal (C, D) sections of dolomitized ACF. The dolomitized ACF are dully-luminescent, whereas the surrounding matrix is luminescent.

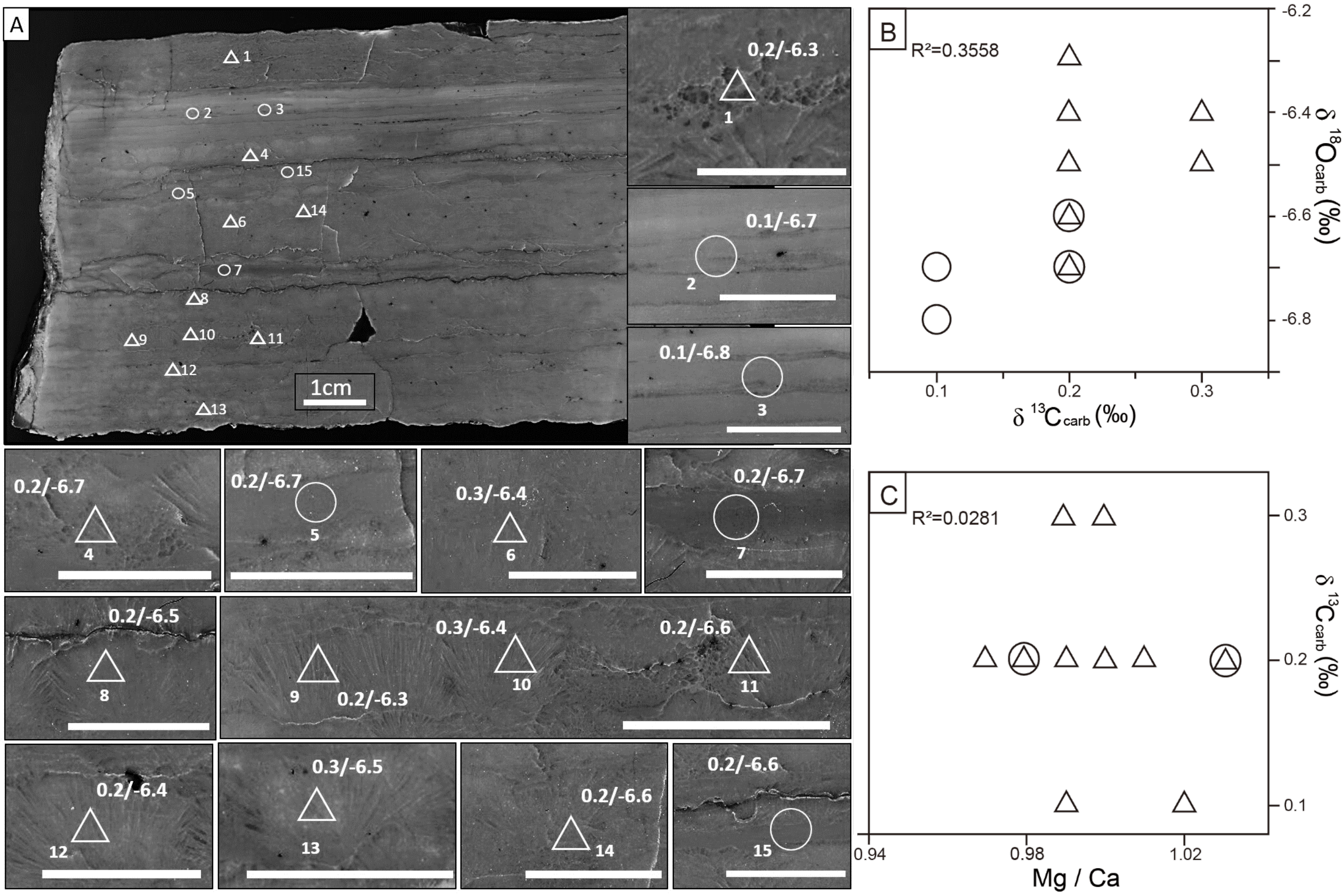

Fig. 11. C and O isotope data for an ACF-bearing slab. (A) Carbonate $\delta^{13}C$ (left) and $\delta^{18}O$ (right) values for dolomitized ACF (triangles) and dolomite matrix (circles) micro-drilled on the slab. The white scale bars are all 1 cm in length. (B-C) Cross plots of $\delta^{13}C_{carb}$ vs. $\delta^{18}O_{carb}$ (B) and Mg/Ca (molar ratio) vs. $\delta^{13}C_{carb}$ (C).

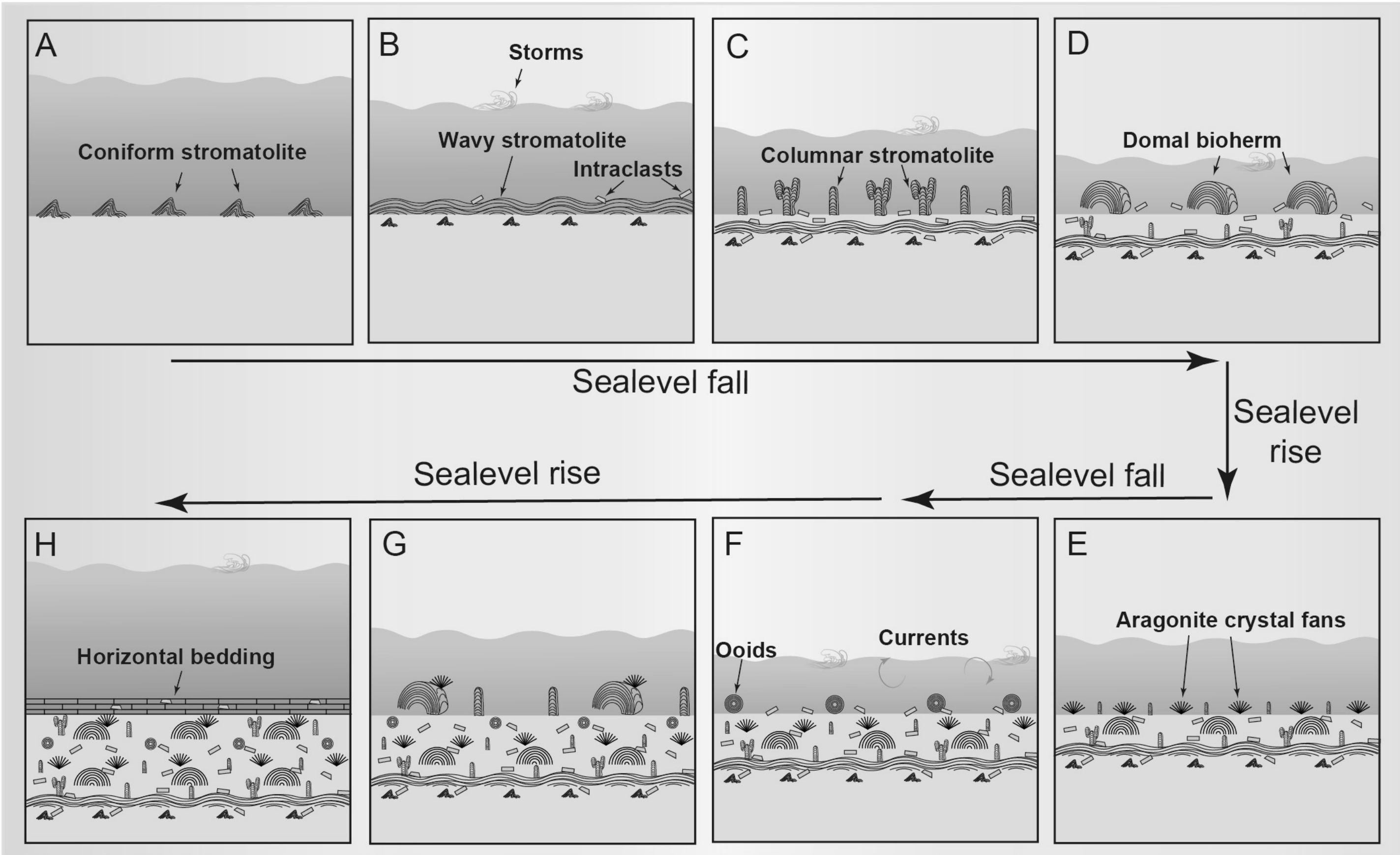

Fig. 12. Cartoons showing a typical depositional cycle in the lower Huaiyincun Formation with an emphasis on the growth of stromatolites and ACF. (A–D) Evolution of stromatolite morphology from coniform to wavy, columnar and domal during the sea level fall. (E –G) Growth of ACF growth on domical bioherms (E, G), formation of ooids (F) and deposition of horizontally bedded dolostone (H) during the subsequent transgression.

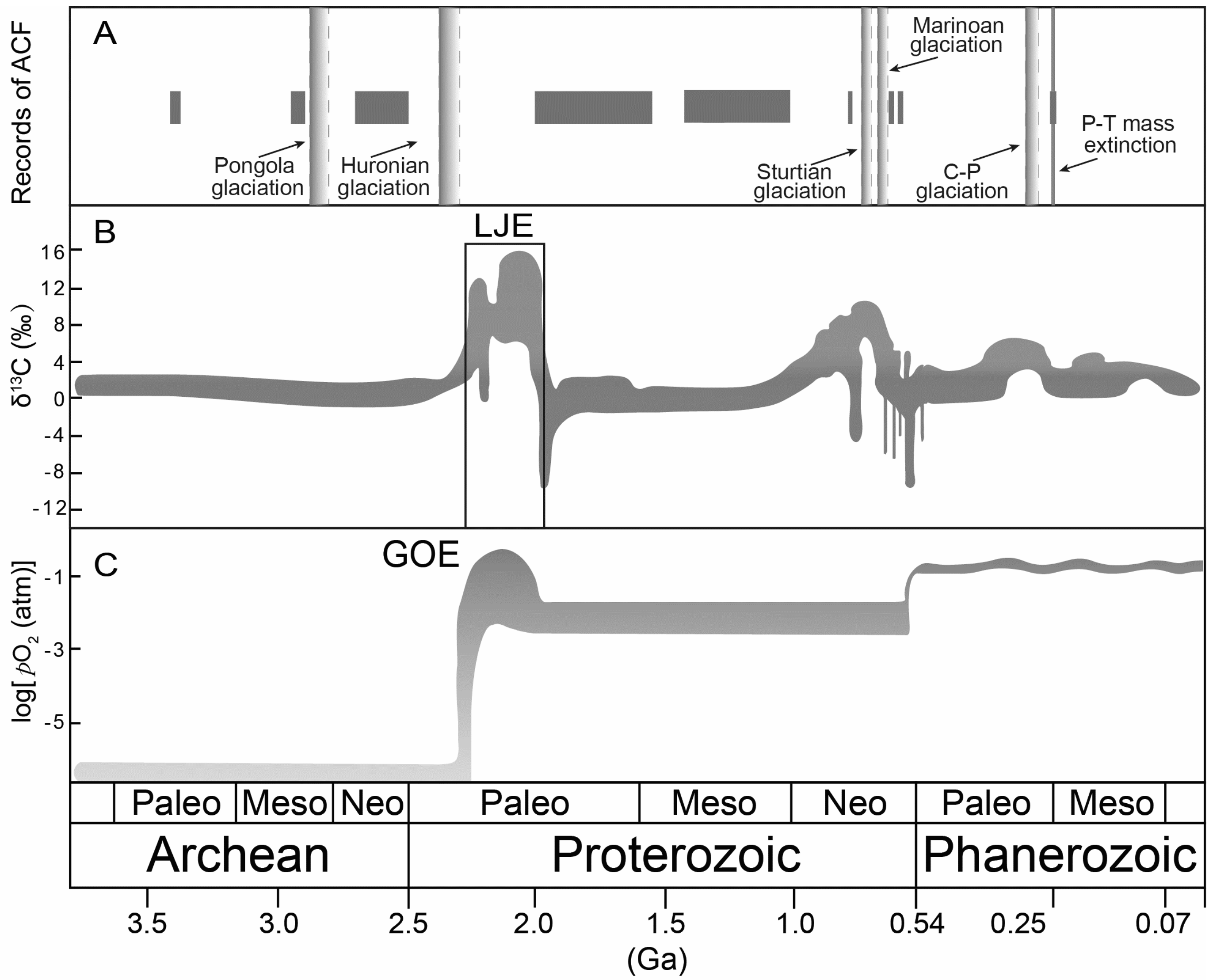

Fig. 13. Occurrences of ACF and glaciations in the geological history (A) and evolution of the carbon cycle (B) and Earth's atmospheric oxygen (C) (B and C modified from Lyons et al., 2014). The dark grey bands in (A) represent unambiguous records of ACF reported in literature and in this study.